Title

Effects of a Dynamical Slab on Back-Arc Melting and Mantle Dynamics

Permalink

https://escholarship.org/uc/item/96g434sg

Author

Brink, Trey

Publication Date

2023

Peer reviewed|Thesis/dissertation

Effects of a Dynamical Slab on Back-Arc Melting and Mantle Dynamics

By

TREY BRINK
THESIS

Submitted in partial satisfaction of the requirements for the degree of

MASTER OF SCIENCE

in

GEOLOGY

in the

OFFICE OF GRADUATE STUDIES

of the

UNIVERSITY OF CALIFORNIA

DAVIS

Approved:

_____

Magali Billen, Chair

_____

Max Rudolph

_____

Barbara Ratschbacher

Committee in Charge

2023

Abstract

Back-arc spreading centers are unique tectonic environments where flux/hydrous melting at the arc occurs in close proximity to decompression melting observed at the back-arc. Numerical geodynamic models of back-arc spreading centers are constructed in order to describe the relationship between kinematically applied surface velocities and anhydrous melt formation, depletion, mantle flow, and slab dynamics. By tracking the evolution of the upwelling region, melt region, and depletion through time, we find that melt area and maximum melt fraction in back-arc spreading centers is primarily related to the back-arc spreading rate. Additionally, while having a smaller upwelling region than mid-ocean ridges with identical spreading rates, back-arc spreading centers have faster upwelling velocities due to flow geometry constrained by the adjacent sinking slab. Likewise, the geometry of the subducting slab is found to have a secondary effect on melt generation within the back-arc spreading center, with a nearly vertically sinking slab resulting in a ~1% increase in maximum melt fraction, especially early on in back-arc spreading. And finally, with the incorporation of two-phase flow, are able to generate oceanic crusts of thicknesses between 7 and 15 km within the back-arc using lower mantle potential temperatures than previous models and neglecting water. This suggests that incorporation of two-phase flow is essential for future models to accurately link melting, crust formation, fluid fluxes, and geochemistry.

Introduction/Background

Back-arc basins are oceanic spreading centers that typically initiate within the volcanic arc above a subducting plate: there are currently ~31 active and inactive back-arc spreading centers (BASCs) on the surface of the Earth, with most active BASCs found in the Western Pacific (Artemieva, 2022). BASCs can form when there is sufficient extension in the overriding plate to induce seafloor spreading, however not all subduction zones have a BASC or even back-arc extension. This extension can be accommodated by trench rollback, either initiated by mantle flow (Tatsumi et al., 1990) or the gravitational instability of the slab (Garfunkel et al., 1986), by far-field overriding plate motion away from the trench (Sholz and Campos, 1995; Nakakuki and Mura, 2012), or by an instability initiated by the removal of the high viscosity boundary layer between the warm mantle wedge and weak, metasomatized crust (Billen, 2017).

As an illustration of BASC geometry, the bathymetry, plate boundaries, and plate ages of the Mariana BASC are shown in Figure 1. The Mariana BASC has had two episodes of back-arc spreading. The Parece Vela Basin (PVR) first episode of back-arc spreading - initiating in the arc and splitting it to form the Palau-Kyushu Ridge (PKR) and West Mariana Ridge (WMR). That spreading initiated at 30-25 Ma. The second episode started at 3-4 Ma, again splitting the active arc separating the West Mariana Ridge from the Mariana Arc (MA) along the Mariana Trench (Artemieva, 2022). Since 6 Ma, the Mariana Trough (MT) has had an average spreading at a rate of 4.3 cm/yr and is currently located at a maximum of ~100 km from the Mariana Arc (Artemieva, 2022).

In these unique tectonic environments, decompression melting at BASCs occurs in close proximity to flux and hydrous melting within the mantle wedge beneath the volcanic arc, and in early stages of back-arc basin evolution these melt regions overlap (Magni, 2019). As a result of this proximity, rocks with trace element patterns between that of MOR basalts and volcanic arc rocks are observed (Fryer et al., 1982; Kelley et al., 2006). Erupted magmas provide information on the source mantle composition, presence of fluids, and PT conditions during melting (Hochstaedter et al., 2000, Kelley et al., 2006).

Additionally, back-arc spreading modifies mantle flow patterns by altering the effective viscosity and advecting heat with the migrating melt (Hall et al., 2012; Magni, 2019). Observations of erupted magmas at BASCs show that there is a large gradient in H_2O concentration and geochemical tracers in the melting source between the arc volcano region and BASC (Kelley et al., 2006; Langmuir et al., 2006; Hochstaedter et al., 2000), suggesting the melt regions of the volcanic arc and back-arc interact and evolve together. Thus, a better understanding of the dynamics of the melt system could help link surficial observations to the driving mantle processes.

Many of the BASC models agree to a first order with the geochemical data from back-arc basin basalts. Models by Hall et al., (2012) find that with the onset of back-arc spreading, temperatures in the mantle wedge increase due to the influx of hot, albeit depleted, mantle material being advected from the BASC to the mantle wedge. Similarly, Magni (2019) shows that there is a decrease in arc magmatism following the onset of back-arc spreading due to the supply of mantle being partially depleted by the back-arc melting. The Hall et al., (2012) study also mimics the pattern of increasing depletion in back-arc basin basalts with increasing back-arc distance, as the mantle beneath these regions becomes progressively depleted due to continued decompression melting. This is consistent with the trace element pattern seen in island arc basalts with an associated BASC, which are depleted in incompatible elements relative to Island arcs without a BASC (Woodhead, et al., 1993).

Current numerical models of melting in back-arc spreading centers (BASCs) have two end member styles (Table 1). The first type are fully kinematic models that prescribe the plate velocities and BASC rates both at the surface and in the slab (Harmon & Blackman 2010; Lin et al., 2010; Hall et al., 2012; see e.g., Figure 2). These kinematic conditions set up mantle flow to generate a BASC. Generally, this style of modelling seeks to find the relationship between subducting plate velocities and BASC rate to melt generation and depletion in the mantle, and whether these imposed conditions can explain geochemical observables. However, the complete kinematic nature of these models prevents the system

4

from evolving dynamically through time and the resulting feedbacks from this behavior on mantle flow patterns is neglected, possibly impacting the location of melt formation.

The second type of BASC models are fully dynamic models (Figure 3). These models start with a protoslab that sinks due to its negative buoyancy and have a model geometry and rheological conditions that promote trench rollback, which induces back-arc basin formation (Nakakuki & Mura, 2012; Magni, 2019). Because the models are allowed to vary through time, they can assess the time-dependence of the dynamics and are much more analogous to what happens in nature. However, the complete dynamic nature of these models makes it difficult to assess relationships between surface plate velocities and locations and volumes of melt. Additionally, they focus heavily on studying the conditions of back-arc basin formation, rather than how this melting evolves for different kinematic conditions.

There is a lack of models that explore a combined approach that can facilitate better understanding of the feedbacks between slab dynamics, surface motion, and melting. Using controlled surface kinematics, while allowing for the slab to evolve dynamically as it subducts into the mantle is currently an unexplored parameter space in the BASC models. This style of modeling will likely lead to a time dependent rate of melting and melt migration, due to slab dynamics influencing mantle flow and the increasing distance between the back-arc and volcanic arc as the model evolves. This will allow the linking of dynamic mantle processes to kinematic conditions observed at the surface.

Furthermore, with the exception of Harmon and Blackman (2010) who incorporate the buoyancy effects of the magma, most models calculate melt as a post-process step. This neglects the compaction pressure resulting from the interaction of the melt and the matrix it resides in, which can affect the path of melt migration and melt production. The post-processing results of these previous models (Table 1) only give snapshots of where melt would be generated given the P-T-H_2O conditions in each model, which is useful for first order results of where melt would form in a real subduction zone and its composition at each instant of time but does not give information on the feedbacks between the melt dynamics and mantle flow (Hall et al.,2012; Magni, 2019).

Another difference between our models and previous modeling efforts is that our models incorporate two-phase flow. This means that the melt and solid are able to flow separately from each other, as the fluid and solid can be subject to different pressure gradients. This prevents the fluid from being entrained within the solid and just advected along the solid velocity path. However, this difference in pressures results in a compaction pressure (Equation 2) between the solid matrix and melt found within the pore space (McKenzie, 1984). Positive compaction pressures can expel melt from the surrounding pore space, while negative compaction pressures can dilate the matrix and induce inflow of melt. The effects of compaction pressure are included in mantle wedge models with two-phase (volatile and rock) Wilson et al. (2014) who found that there is a flow focusing effect of fluids. That is, fluids will tend to travel along paths it has already traveled. Similar results have been documented in mid-ocean ridge spreading models (e.g., Sim et al., 2020). In BASC models, this likely results in a greater melt fraction near the center of spreading, and smaller melt fractions at the edge.

This project aims to act as a starting point to fill the aforementioned gap in models and to demonstrate what can be done in ASPECT using the current implemented melt model, which incorporates the coupled dynamics between the melt and the mantle it resides in with a dry formulation for melting (Katz et al., 2003; Dannberg and Heister, 2016).

Methods

Two-dimensional box models of a subduction zone with an associated BASC is created using the open source modeling software ASPECT (Kronbichler et al., 2012; Heister et al., 2017; Bangerth et al., 2021a; Bangerth et al., 2021b; Dannberg and Heister, 2016; Fraters et al., 2019; Fraters, 2010). ASPECT permits a coupled dynamic-kinematic approach allowing for set surface kinematics with a dynamically evolving slab and mantle flow. To do this, ASPECT numerically solves conservation of momentum, mass, and energy for highly viscous flows.

Model dimensions used in this study are 4500 km in width by 3000 km depth. The depth and width is chosen to approximate that of the core-mantle boundary while minimizing edge effects in the center of the domain. Figure 4a shows the model domain. The mesh has varying element sizes between the coarsest mesh in the lower mantle of ~23 km and the finest mesh of ~0.7 km in the shear zone (Figure 4). The shear zone is necessary to decouple the overriding plate and subducting plate and represents the megathrust fault. Additionally, there is a higher resolution of ~2.8 km at the surface and ~1.4 km near the trench and BASC. Figure 4b shows the mesh near the trench. The initial temperature model for the overriding plate is a half space cooling model of a 50 Myr oceanic plate that thins as it approaches the trench. Similarly, the initial temperature profile of the subducting plate is that of a half space cooling model with a ridge positioned at a distance outside the box chosen to fix the subducting plate age at a given plate velocity. The mantle initial temperature profile is adiabatic. The models have a uniform initial composition of peridotite but do track depletion due to melting and crystallization. Initial temperature and composition geometry are defined using Geodynamic World Builder (Fraters et al., 2019; Fraters, 2020) as a plugin to ASPECT.

The surface traction boundary conditions are adapted from Hall et al. (2012) and are used to drive subduction at a convergence rate $\mathbf{u}_c$ and a back-arc spreading center that migrates away from the volcanic arc at half the total back-arc spreading rate $\mathbf{u}_b$ (Figure 5a). The model has two stages: (1) the first stage acts as a set-up phase, in which a protoslab is subducted until it passes through the 660 km boundary, and (2) the second stage initiates back-arc spreading by applying a surface velocity away from the trench in the arc region that migrates away at a rate of ½ $\mathbf{u}_b$ (Figure 5b). The first stage allows for the creation of a dynamic starting point for back-arc spreading. During both stages of modeling, anhydrous melting is able to occur, but in all models only forms after the initiation of back-arc spreading in Stage 2. These boundary conditions result in trench retreat relative to the overriding plate, however the location of the trench is stationary within the reference frame of our model. The side boundary conditions are open, meaning that

a reference lithostatic pressure profile is determined at each depth and is applied as the pressure on the side walls. This allows for the mantle to flow in and out freely. The bottom is free slip.

A suite of 31 different models varying Slab Age at the trench A, convergence rate $\mathbf{u}_c$, and back-arc spreading rate $\mathbf{u}_b$ is used to investigate how these parameters affect melting in the BASC. Models with a convergence rate of 7 cm/yr or larger were ran with a 400 km longer protoslab, as this was necessary to initiate subduction. Additionally, 2 models are ran without a slab and no applied convergence velocity as an isolated MOR; these reference models allow the effect of the nearby slab to be determined. Table 2 lists a summary of the parameter values used for each model.

To include anhydrous melting in our models, we use a modified version of the Melt Simple material model within ASPECT (Dannberg and Heister, 2016). Melt Simple solves a modified version of conservation equations that incorporate melting, crystallization, and melt transport originally derived by McKenzie (1984). This was reformulated by Dannberg and Heister (2016) giving the following expression for conservation of momentum

$$-\nabla\left[2\eta\left(\dot{\varepsilon}(\boldsymbol{u_s}) - \frac{1}{3}(\nabla \cdot \boldsymbol{u_s})\mathbf{1}\right)\right] + \nabla p_f + \nabla p_c = \bar{\rho}\boldsymbol{g}, \tag{1}$$

where η is the shear viscosity, $\dot{\varepsilon}$ is strain rate, $\boldsymbol{u_s}$ is solid velocity, p_f is fluid pressure, p_c is compaction pressure, $\bar{\rho}$ is mean density of the fluid and solid, and $\boldsymbol{g}$ is acceleration due to gravity. This equation states that the stresses in the solid, in addition to the pressure gradients, are balanced by the gravitational body force. It represents a combined conservation of momentum for the fluid and solid utilizing compaction pressure, which is

$$p_c = (1 - \phi)(p_s - p_f). \tag{2}$$

where ϕ is porosity. Combining these two pressure terms into a single compaction pressure term allows for a more efficient solver and gives more insight into the dynamics of solid-melt interaction by

8

describing pressures exerted on the solid by the fluid and vice versa (Dannberg and Heister, 2016; Keller et al., 2013). The original conservation of mass equations for the fluid and solid from McKenzie (1984) are as follows

$$\frac{\partial}{\partial t}[\rho_f \phi] + \nabla \cdot [\rho_f \phi u_f] = \Gamma, \tag{3}$$

$$\frac{\partial}{\partial t}[\rho_s(1-\phi)] + \nabla \cdot [\rho_s(1-\phi)u_s] = -\Gamma, \tag{4}$$

where ρ_f is fluid density, ρ_s is solid density, Γ is melting rate, and u_f is fluid velocity. These equations indicate that the mass of the fluid/solid at a given point are due to the divergence of the respective mass flux and melting rate. Dannberg and Heister (2016) combine equation (3) and (4) and utilize Darcy's Law to remove the fluid velocity term $\boldsymbol{u_f}$ to reach the following formulation for the conservation of mass for fluid and solid used in ASPECT

$$\nabla \cdot \boldsymbol{u_s} - \nabla \cdot K_D \nabla p_f - K_D \nabla p_f \cdot \frac{\nabla \rho_f}{\rho_f} = \tag{5}$$

$$-\nabla \cdot \left(K_D \rho_f \boldsymbol{g}\right) + \Gamma\left(\frac{1}{\rho_f} - \frac{1}{\rho_s}\right) - \frac{\phi}{\rho_f}\boldsymbol{u_s} \cdot \nabla \rho_f - (\boldsymbol{u_s} \cdot \boldsymbol{g})(1-\phi)\kappa_s \rho_s - K_D \boldsymbol{g} \cdot \nabla \rho_f,$$

where K_D is the Darcy coefficient (ratio of permeability to fluid viscosity) and κ_s is the isothermal compressibility of the solid. Additionally, a constitutive law for compaction stresses in the solid rock is needed

$$\nabla \cdot \boldsymbol{u_s} + \frac{p_c}{\xi} = 0, \tag{6}$$

where ξ is the bulk viscosity of the solid. Using equations (1), (3), and (4), ASPECT solves for solid velocity $\boldsymbol{u_s}$, compaction pressure p_c, and fluid pressure p_f (Dannberg and Heister, 2016). Additionally, when porosity is 0, these equations reduce to the normal conservation equations solved by ASPECT. The last governing equation ASPECT uses in Melt Simple is energy conservation is:

$$\bar{\rho} C_p \left(\frac{\partial T}{\partial t} + \boldsymbol{u_s} \cdot \nabla T \right) - \nabla \cdot k\nabla T = 2\eta(\dot{\varepsilon}_s : \dot{\varepsilon}_s) + \alpha T(\boldsymbol{u_s} \cdot \nabla p_s) + T \, \Delta S \, \Gamma \tag{7}$$

where C_p is specific heat, k is permeability, $\dot{\varepsilon}_s$ is shear strain rate, and ΔS is entropy change. The LHS contains the heat capacity term and conduction term. The RHS contains the viscous dissipation, adiabatic heating, and latent heat of melting/crystallization terms. Parameters used in the modeling are given in Table 3. Model output that we visualize are melt fraction, depletion (modeled as the fraction of the source rock that has already been molten), the solid velocity field, and compaction pressure.

Shear Viscosity Model

The Melt Simple material model uses a solid shear viscosity that is only dependent on temperature and porosity and has the form:

$$\eta(\phi, T) = \eta_0 exp(\alpha_0 \phi) exp\left(\frac{-\beta(T - T_{adi})}{T_{adi}} \right) \tag{8}$$

where η_0 is the reference shear viscosity, α_0 is the exponential melt weakening factor, β is the thermal viscosity exponent, and T_{adi} is the adiabatic temperature at a given depth. This, by itself, leads to a viscosity that decreases with depth when using an adiabatic temperature model.

We make four main changes to the original solid shear viscosity model. First, we added a depth-dependent viscosity factor

$$\theta_d = \begin{cases} m_1 z, & 66 < z < 660 \\ m_2 z + b, & 660 \le z < 3000 \end{cases} \tag{9}$$

where m_1 is the slope for the upper mantle, m_2 is the slope for the lower mantle, z is depth in km, and b is the offset between the upper and lower mantle. θ_d increases linearly with depth, which is necessary to counteract the decrease in viscosity with depth in the original formulation. Second, we include a temperature offset factor T_{offset} to shift the entire viscosity profile to be more viscous, which is important for creating a highly viscous slab while maintaining a weaker upper mantle. Third, we increase the viscosity limiter by a factor of 10, allowing for a larger range in slab viscosities and up to 1e23 Pa s at

the surface. Slab viscosity can exceed this value with depth, as it is affected by the depth-dependent viscosity factor. Our reformulation is expressed as

$$\eta(\phi, T) = \eta_0 \theta_d \exp(\alpha_\phi \phi) \exp\left(\frac{-\beta(T - T_{adi} - T_{offset})}{T_{adi} - T_{offset}}\right) \tag{10}$$

And finally, we create a 10-km thick shear zone above the slab extending to ~100 km that overrides all viscosity changes and imposes a constant viscosity, $\eta_{sz} = 1e20$ Pa s which is necessary to decouple the subducting and overriding plates. An example viscosity profile is shown in Figure 6. Note that this viscosity formulation does not account for stress-dependent (i.e., dislocation creep), grain size dependence, water dependences, or plasticity in the slab. The implications of these simplifications are considered in the discussion.

Anhydrous Melting

Melt Simple uses the Katz et al., (2003) parameterization of anhydrous melting, which was also used in previous studies of melting in BASCs (Harmon & Blackman, 2010; Hall et al., 2012; Magni, 2019) and MORs (Sim et al., 2020). The values of the parameters in the following equations are given in Katz et al., (2003) and are used without any changes. This implementation uses a set of quadratic equations to approximate the solidus, lherzolite liquidus, and true liquidus in the form

$$T_{solidus} = A_1 + A_2 P + A_3 P^2, \tag{11}$$

$$T_{liquidus}^{lherz} = B_1 + B_2 P + B_3 P^2, \tag{12}$$

$$T_{liquidus} = C_1 + C_2 P + C_3 P^2, \tag{13}$$

where T is temperature in Kelvin, P is pressure in GPA. The equations are plotted in Figure 7. Then, the fractional distance between these melting curves is used to determine melt fraction as follows

$$F_{cpx}(T) = \left[\frac{T - T_{solidus}(P)}{T_{liquidus}^{lherz}(P) - T_{solidus}(P)}\right]^{\beta_1}, \tag{14}$$

where cpx denotes that this is melting prior to the depletion of clinopyroxene and β_1 is a power law scaling factor. A similar equation can be written for melt fraction following the depletion of clinopyroxene and the melting reaction begins utilizing mostly orthopyroxene

$$F_{opx}(T) = F_{cpx-out} + \left(1 - F_{cpx-out}\right)\left[\frac{T - T_{cpx-out}}{T_{liquidus} - T_{cpx-out}}\right]^{\beta_2}, \tag{15}$$

with

$$F_{cpx-out} = \frac{M_{cpx}}{R_{cpx}(P)}, \tag{16}$$

where $F_{cpx-out}$ is the melt fraction at which clinopyroxene is depleted, M_{cpx} is the weight fraction of clinopyroxene in the solid being isobarically melted, and $R_{cpx}(P)$ is the pressure dependent reaction coefficient for clinopyroxene. Also, from equation (15),

$$T_{cpx-out} = F_{cpx-out}^{\frac{1}{\beta_1}}\left(T_{liquidus}^{lherz} - T_{solidus}\right) + T_{solidus}, \tag{17}$$

with $T_{cpx-out}$ being the temperature at which clinopyroxene becomes depleted. A dry melting curve can be seen in Figure 8.

Given this set of equations for anhydrous melting, the primary mechanisms in which melting can occur in a given parcel of material is through increasing its temperature or decreasing its pressure. In our models, we expect that the primary mechanism through which melting will occur is by decreasing the pressure. In back-arcs the primary mechanism of melting is decompression, and so the melting rate is directly related to the upwelling velocity, area that is upwelling, and temperature of the upwelling material.

Hydrous Melting

Hydrous melting, while not currently implemented in Melt Simple, is critically important next step to these models and so is described here following Katz et al. (2003). Additionally, the Hall et al. (2003) and Magni (2019) account for the presence of water, another important factor affecting total melt

and crust formation (Table 1). Hydrous melting is incorporated by reusing the anhydrous equations (6),

(7), and (8) by incorporating a temperature decrease in each solidus and liquidi equation as a function of

the weight fraction of water (X_{H_2O}) in the melt in the form

$$\Delta T(X_{H_2O}) = K X_{H_2O}^{\gamma}, \tag{18}$$

where K and γ are reaction parameters used to calibrate this function. At higher water contents, the melt

system can be saturated such that the addition of more water will not produce any more melting. Water

saturation as a function of pressure is as follows

$$X_{H_2O}^{sat} = \chi_1 P^{\lambda} + \chi_2 P, \tag{19}$$

where χ_1, χ_2, and λ are reaction parameters used to calibrate this function. It is important to note that

X_{H_2O} represents water content within the melt and not the entire system as is represented by $X_{H_2O}^{bulk}$.

Starting from the $X_{H_2O}^{bulk}$ assigned in the model, we then need an equation to partition water between the

solid and the melt. It is modeled as follows

$$X_{H_2O} = \frac{X_{H_2O}^{bulk}}{D_{H_2O} + F(1 - D_{H_2O})}, \tag{20}$$

where D_{H_2O} is a bulk distribution coefficient. And finally, with this the total melting function can be

written as

$$F(P, T, X_{H_2O}^{bulk}) = \left[\frac{T - \left(T_{solidus} - \Delta T\left(X_{H_2O}(X_{H_2O}^{bulk}, P, F) \right) \right)}{T_{liquidus}^{lherz} - T_{solidus}} \right]^{\beta_1} \tag{21}$$

for $F \leq F_{cpx-out}$. The equation for hydrous melt fraction has no analytical solution and must be solved

numerically. A similar equation can be written for $F > F_{cpx-out}$. Figure 8 shows the effect of

incorporating water in melt, as it drastically lowers the temperature needed for melting, which is

especially apparent at lower melt fractions. This implementation of melting has been widely adopted in

BASC models (Harmon and Blackman, 2010; Hall et al., 2012; Magni, 2019; see Table 1), as it is

straightforward to implement and computationally inexpensive. Future models building on the results presented here could start by implementing these hydrous melting equations in ASPECT.

Results

A suite of numerical models of back-arc spreading centers were created in order to test the effects of surface kinematic conditions on anhydrous melt formation, depletion, slab dynamics, and mantle flow patterns. For this suite, we varied convergence velocity $\mathbf{u}_c$ between the range of 3 cm/yr and 9 cm/yr, back-arc spreading rate $\mathbf{u}_b$ between the range of 2.5 cm/yr and 7.5 cm/yr, and plate age at the trench between 50 Myr and 90 Myr. Additionally, two test models (Model 1 and 2) with no slab are created in order to act as a test case to ascertain the effects of the slab in the other models. These two models are essentially a MOR that slowly migrates within the reference from of the model. Table 2 summarizes all models ran in this study.

We first show a half-space cooling model used to demonstrate anhydrous melting calculated solely on P-T conditions and then the two MOR-style models. These two models act as a comparison for the rest of the models, which is important for distinguishing the differences between melting in MOR systems and BASC systems. Then, we show the influence of the BASC on mantle flow and slab dynamics by looking at the time evolution of flow and slab motion. And finally, we look at melt formation and depletion, as melt formation is controlled by the location of the hot upwelling mantle material beneath the BASC.

Mid-Ocean Ridge with no Slab

In order to demonstrate the effects of anhydrous melting with no feedback between the solid and melt, we construct a half-space cooling model and calculate melt fraction with depth for plates ages between 2 and 8 Myr (Figure 9). We use the same mantle potential temperature of 1570 K here as in the rest of our BASC and MOR models. In these models, we find that at 2 Myr, the melt fraction reaches a

maximum of ~14% and that beyond 8 Myr, the melt fraction reaches 0. Furthermore, the depth of the maximum melt increases through time. This is similar to what we see within our MOR models.

In the MOR models (Models 1 and 2), the overlying plate has an age of 50 Myr and is initially thinned by 15 km in order to replicate the initial thinning of the mantle wedge in the BASC models. After spreading initiates, an upwelling region forms immediately. In our analysis, to help characterize mantle flow, we define the upwelling region as the area with an upward component of velocity greater than 0.5 cm/yr. For the MOR models, this region is broad and is symmetric about the spreading axis. Over time, this upwelling region expands, while the maximum upwelling velocity decreases. As this upwelling region broadens, so too does the melt region. Importantly, without the influence of a subducting slab, the upwelling region is unconstrained and relatively diffuse.

Mantle Flow and Slab Dynamics

The rest of the models, while having the same spreading surface boundary conditions, also incorporate a slab that sinks alongside the back-arc spreading. As spreading in these models commence, it creates a pressure gradient towards the BASC that drives mantle flow into this region. This upwelling advects hotter mantle up to shallower depths that have lower pressures, inducing melting. Thus, the location and rate of upwelling is one of the main drivers of decompression melting in these models. These pressure gradients also have an effect on the nearby subducting slab, pulling it towards the back-arc. Figure 11 shows the velocity field responding to the initiation of back-arc spreading. Essentially, both the slab and mantle respond immediately to the initiation of the back-arc spreading.

Fast Convergence Models

In the cases of models with a faster convergence rate of 7 cm/yr or higher and/or a back-arc spreading velocity of 7.5 cm/yr (Models 11 through 31; Table 2), the back-arc spreading center pulled the subducting slab through the shear zone at shallow depth. An example of this can be seen in Figure 12. This is a byproduct of the Newtonian viscosity we use in our models (Billen and Hirth, 2005) and indicate

the slab can be strongly affected by the initiation of the BASC. However, because these models pass through the shear zone, rather than sinking, they cannot be used for further analysis. Future models will need to incorporate non-Newtonian mantle viscosity to explore BASC at faster convergence and spreading rates.

Slow/Intermediate Convergence

In the remaining slow/intermediate models (Models 1 through 10; Table 2), back-arc spreading still has a considerable effect on the slab, but not enough to pull it through the shear zone as in the fast convergence models. Similar to in the MOR models, we track the evolution of upwelling region (e.g., Figure 13 for Model 8). Before back-arc spreading initiates, the upwelling region is comparatively small and has slower upwelling velocities that do not generate melt. However, once back-arc spreading is initiated the upwelling in the BASC models are smaller, faster, and asymmetric as compared to the MOR models. Over time, as the BASC moves away from the arc, and the upwelling region grows in size and becomes more diffuse, resulting in slower upwelling velocities.

Plots of upwelling velocity, upwelling area, and total upwelling versus back-arc spreading distance are shown in Figure 14. Early on, all models undergo a rapid increase in average upwelling velocity until ~100 km of back-arc spreading has occurred. After this point, average upwelling velocities decay. This decay in velocity corresponds to an increase in size of the upwelling region. Average upwelling velocities and areas depend mostly on back-arc spreading rate. Additionally, slab age appears to have a minor control early on in BASC spreading, with older slabs having both a faster and larger area of upwelling before being matched or overtaken by the younger slabs. These results suggest that there is a distance at which the BASC becomes geometrically far enough away from the slab and behaves more like a MOR.

Also, during this time, the slab is pulled forward by the same pressure gradients driving the upwelling region. This motion can be seen happening to the slab in Figure 13. To quantify how the slab

responds to these changes initiated by back-arc spreading, we measure the angle of sinking within the slab (CCW from horizontal). We measure the angle of sinking between the depths of 150 km and 550 km and use a temperature threshold of 1300 °C to differentiate the mantle and slab (Figure 11). Figure 15 shows the angle of sinking in the slab as back-arc spreading proceeds. The angle of sinking immediately prior to back-arc spreading is plotted as a dot for each set of convergence velocity and plate age (from dot to start of corresponding curve) Initially, there is a large decrease in the angle of sinking following the onset of back-arc spreading, that over time increases again as the back-arc becomes more distant. An interesting deviation from this trend is seen in Model 8 where the angle decreases slightly after ~320 km of back-arc spreading and is the result of a minor slab buckling at 400 km depth. This buckling creates a slightly steeper region above 400 km depth that beyond which, gradually increases to the 660 km boundary. The 3 cm/yr convergence velocity models have the greatest decrease in the angle of slab sinking following the initiation of back-arc spreading, and then the most rapid increase in angle of sinking as back-arc spreading commences. This is due to the near vertical sinking of the slab and slower convergence reducing the pressure gradient pulling the slab toward the BASC. Additionally, older slabs are more resistant to the change in angle after the onset of back-arc spreading due to their increased thickness and density making them more resistant to changes in motion.

Taken together, the applied back-arc spreading surface velocities are the primary control of upwelling within the mantle. Additionally, the geometry of the slab localizes mantle flow and the slab itself pulled in the direction of back-arc spreading. The effect on the slab seen in the slow/intermediate velocity models is essentially a less extreme version of the fast convergence models being pulled through the shear zone. And finally, slab geometry prior to the initiation of back-arc spreading plays an important role in the upwelling velocities, as a steeper slab allows both for mantle from greater depths to reach beneath the BASC more easily, as well as geometrically having more space for the mantle to flow in and out of the BASC.

Melting and Depletion

The upwelling region determines the location of melt formation, and its general shape as can be seen in Figure 10 for the MOR and Figure 13 for the BASC. Evolution of just the melt regions can be seen in Figure 16. The main difference between the melt regions in the MOR compared to the BASC is the asymmetry that develops with a longer 'tail' on the arc side of the melt region. Additionally, the models with a slower back-arc spreading rate (e.g., Figure 16c) have a much smaller melt extent and maximum melt fraction, which corresponds to the decreased upwelling velocities (Figure 14). Additionally, the main region of melt formation is between ~14-60 km depth, with 2.5 cm/yr back-arc spreading models having a smaller range of melt formation at depths between 20-54 km. Above the region of melt formation, crystallization occurs over a much narrower 2-3 km depth range.

In Figure 17, we sum all melt present in the model and plot it over back-arc spreading distance. The primary control on melt formation is back-arc spreading rate. Secondary to this, the MOR models developed greater melt than any of the BASC models aside from early on in Model 4. The reason for this is that Model 4 develops a rapid and localized upwelling region (Figure 14a) that can temporarily outpace the melt formation in the MOR models, which is related to the initially nearly vertically descending slab (Figure 15). Another secondary factor to melt formation is slab age. Older slabs develop more melting than younger slabs, which in these models also seems to be related to slab dip.

Because of the two-phase flow present in these models, melt is able to form, deplete the mantle it formed from, travel towards the spreading axis, and then crystallize, enriching and forming a crustal layer. Also of note is that melt fraction is directly tied to depletion in these models and is modeled as the fraction of the source rock that has already been molten. Figure 18 shows the evolution of depletion through time in both a 5 cm/yr (Model 8) and 2.5 cm/yr (Model 5) back-arc spreading rate model. The faster models develop greater magnitudes of both depletion and enrichment. Here, enrichment is defined to mean the opposite of depletion (e.g., melt crystallization results in enrichment). Additionally, the thickness of the enriched crust that develops ranges from 10-15 km in the 5 cm/yr back-arc spreading rate

18

models and 7-15 km in the 2.5 cm/yr back-arc spreading rate models. In both cases, the crust evolves to be overly thick, in part due to Newtonian rheology of the overriding plate, the surface velocity boundary conditions, and cell size. Another interesting feature that develops is a difference in depth of the enriched region at the axis of the BASC. Because melting is able to occur at shallower depths in the faster back-arc spreading models, the region of enrichment is also shallower.

Figure 19a shows maximum depletion over back-arc spreading distance. For every model, maximum depletion reaches a steady-state after ~200 km of spreading distance and the same goes for maximum melt fraction (Figure 19b). This shows that the increase in total melt (Figure 17) after this point is predominantly due to the melt region expanding which can also be seen in Figure 16. As is the case with total melt, Model 4 develops rapid depletion and melting early on than in the MOR model. Slower back-arc spreading velocity models still maintain a relatively large melt fraction of ~11% at steady-state, only 3% less than the 5 cm/yr spreading rate models. The difference between total melt between slower and faster back-arc spreading models is primarily accounted for in the larger size of the melt area.

Discussion

Together, these results on melting and depletion beneath back-arcs show that while back-arc spreading rate is a primary control on total melt formation, the slab geometry, slab motion, and slab thickness apply a secondary control on anhydrous melt formation in the back-arc by controlling mantle flow. Additionally, they show that depleted material inevitably gets advected beneath the arc and that using two-phase allows for the formation of an enriched crust.

The kinematic nature of the overlying plate motion in these models make them most similar to the mechanism of far-field overriding plate motion away from the trench, because if the extension were driven purely by trench retreat, the back-arc spreading velocity would not have such an effect on the slab dynamics. In the case where trench retreat is driving back-arc spreading, the slab is accommodating the motion of the back-arc extension, rather than the back-arc influencing the slab (Sholz and Campos, 1995).

This study was motivated by the hypothesis that slab dynamics and two phase flow would impact the process of melting at BASCs. These findings corroborate many of the findings seen in previous BASC models (Hall et al., 2012; Magni, 2019) such as the advection of depleted mantle material beneath the arc and general mantle flow pattern during back-arc spreading. The shape of the decompression melt region is similar to that seen in Magni (2019). Additionally, we find that BASC influences its host subduction zone in a variety of ways. First, it influences mantle flow patterns beneath the arc by creating a pressure gradient towards the arc. It also depletes the mantle prior to reaching the arc, in agreement with past geochemical studies that suggest a two-step melting model (Cooper et al.,2010), and with the Magni (2019) study which use tracers to track depletion. An additional factor we find that affects BASC melting is the geometry of the slab. A steeper slab gives a more direct path for deeper mantle material to flow into the back-arc and creates a larger region of upwelling, leading to greater melt formation. This is especially important when the BASC is close to the arc. And while our models don't run long enough for the back-arc to create a separate convection cell, as seen in Magni (2019), that would likely happen as the BASC reaches a critical separation distance away from the arc. However, no BASC has produced a global scale ocean basin, instead creating smaller oceanic microplates (Li et al., 2018).

Additionally, in our models we see the formation of oceanic crust due to changes in the thermal structure of the subduction zone by thinning the overlying crust and supplying hot mantle material beneath the back-arc. A difference between these models and previous studies is that we use a mantle potential temperature ~50 °C less than both Hall et al., (2012) and Magni (2019), leading to smaller melt fractions and thus smaller depletions that get advected beneath the arc. Despite these lower melt fractions, two-phase flow allows for the formation of a sufficiently thick (or overly thick) 7 to 15 km crust of enriched material created at the BASC (Carbotte and Canales, 2019), and demonstrating the importance of two-phase flow in focusing magma flow to where it crystalizes. Additionally, there are other important factors beyond spreading velocity that determine crustal thicknesses in BASCs, such as a heterogeneous

mantle composition (Grevemeyer et al., 2020). Thus, crustal thickness provides an additional

observational constraint we can use to constrain future BASC models.

Future Work and Model Limitations

This project aims to act as a starting point to fill the aforementioned gap in models and to

demonstrate what can be done in ASPECT using the current implemented melt model, which incorporates

the coupled dynamics between the melt and the mantle it resides with a dry formulation for melting (Katz

et al., 2003; Dannberg and Heister, 2016).

This project aimed at exploring a combined modeling approach using kinematically applied

surface velocities and a dynamical slab in order to study mantle flow and anhydrous melting in BASCs

and setting the stage for future BASC modeling using ASPECT. Provided here are limitations to these

models and potential future directions that would greatly enhance the utility of the models, especially for

comparison to a greater array of BASC systems and geological/geochemical/geophysical data.

- A clear limitation of these models is the Newtonian rheology and lack of plasticity. These

  models are only able to look at slow subduction systems with velocities 5 cm/yr or

  smaller. A weaker mantle wedge corner is needed in order to prevent the slab from being

  pulled through the shear zone, and a non-Newtonian rheology would decrease the

  viscosity in regions with a high strain-rate like the mantle wedge (Billen and Hirth,

  2005).

- Another future direction is incorporating hydrous and/or flux melting into these models.

  With that, it would be possible to see how the arc melt region and back-arc melt region

  interact with each other, and then separate as seen in Magni (2019). Additionally, it

  would quantify how the prior mantle depletion would affect the melting beneath the arc.

  To accomplish this, a method to incorporate and track water would be necessary, the use

of a hydrous melt model for peridotite (Katz et al., 2003), and a separate model of flux melting.

- Another limitation in these models is that it is difficult to constrain the effects of the 2-phase flow without the use of a model that does not utilize it, and so in the future a model without the use of 2-phase flow could be developed as a comparison.

- Another relatively simple test could be done to determine the effects of mantle potential temperature more precisely on melt formation, depletion beneath the arc, and the thickness of the enriched crust. Observations of crustal thickness as a function of spreading rate could be used to constrain the potential temperature in BASC systems.

- The kinematic nature of back-arc spreading in these models likely result in a BASC that has more influence on slab dynamics than it otherwise would. The slab in our models was greatly affected by the initiation of the BASC, which is also in part due to the Newtonian rheology. A possible direction would be to develop dynamically initiated BASC models. For example, by applying far field plate motions and an initial "weak" region in the arc.

- Another area that can be expanded on is adding in geochemical tracers to represent large ion lithophile elements and high field strength elements (Woodhead et al., 1993). This would allow for more direct comparison to geochemical studies of volcanic arc and back-arc basin rocks (Woodhead et al., 1993; Kelley et al., 2006; Langmuir et al., 2006; Hochstaedter et al., 2000).

Conclusion

In this study, we use 2D models of BASCs to test the implementation of two-phase flow and anhydrous melting within ASPECT and to investigate how convergence rate, back-arc spreading rate, and slab age at the trench influence mantle flow patterns, melt formation, and depletion within the mantle wedge and beneath the BASC. We find that with its current implementation in ASPECT, Melt Simple cannot be used to model faster (> 5 cm/yr convergence and back-arc spreading rates) back-arc systems and a new formulation for shear viscosity is needed to do so. Additionally, we determine that slab geometry acts as a secondary effect in melt generation, as a steeper slab essentially allows for deeper, hotter mantle to more easily be pulled beneath the BASC and to allow for greater space for upwelling. And finally, we find that the implementation of two-phase flow allows for the use of crustal thicknesses as an additional observational constraint in models of back-arc spreading centers.

Appendix

Code overview

This section contains an explanation of the following files used to create the models outlined in this thesis:

- The worldbuilder file used to create the initial conditions in the models.

- The ASPECT parameter files used in the models.

- The changes made to the code within the Melt Simple material model.

The Stage 1 parameter file initializes subduction starting with a proto-slab and an overlying plate. We use Geodynamic Worldbuilder to set the initial temperature conditions of the slab, slab plate, and overriding plate independently of the adiabat that we generate using ASPECT. Additionally, worldbuilder is used to set the location of the shear zone, which is assigned as a compositional field in ASPECT and is recognized by the Melt Simple material model which assigns it a fixed viscosity.

Worldbuilder File

Here I will go over the worldbuilder file used for the 50 Myr, 5 cm/yr convergence velocity models. Note that the worldbuilder file is only used in the Stage 1 models, as it supplies the initial conditions of the model.

```
{
  "version":"0.5",
  "coordinate system":{"model":"cartesian"},
  "cross section":[[0,0],[4500e3,0]],"surface temperature":273, "force surface temperature":false,
  "potential mantle temperature":1570, "thermal expansion coefficient":3e-5,
  "specific heat":1250, "thermal diffusivity":1.0e-6,
```

Worldbuilder works in three-dimensions, and our models are all two dimensional slices of that 3D domain (Figure A1). We create a slice through that domain for these 2D models using the "cross section" field. Additionally, here we define physical constants needed to create the temperature structure of the model.

```
"features":
[
  { "model":"oceanic plate", "name":"imaginary", "max depth":150e3,"min depth":0,
    "coordinates":[[2000e3,-100e3],[2000,100e3],[2500e3,100e3],[2500e3,-100e3]],
    "temperature models":[
      {"model":"half space model",
       "min depth":-10e3,  "max depth":150e3, "spreading velocity":0.01,
       "top temperature":273, "bottom temperature":-1,
       "ridge coordinates": [[[2000e3,-100e3],[2000,100e3]]] }]},
```

Next, we move into model "features", which include oceanic plates and the protoslab in our model. First, we define an oceanic plate with a ridge centered at 2000 km in our model (1 in Figure A1). This is used to create a temperature structure in the plate above the mantle wedge that thins as it approaches the mantle wedge corner. This is defined first, as worldbuilder will overprint the following features overtop of this, leaving behind only the section of the plate that thins towards the mantle wedge corner.

```
  { "model":"oceanic plate", "name":"Y-ridge", "max depth":150e3,"min depth":0,
    "coordinates" :[[2500e3,1000e3],[4500e3,1000e3],[4500e3,-100e3],[2500e3,-100e3]],
    "temperature models":[
      {"model":"half space model",
       "min depth":-10e3,  "max depth":150e3, "spreading velocity":0.01,
       "top temperature":273, "bottom temperature":-1,
       "ridge coordinates": [[[2500e3,500e3],[4500e3,500e3]]] }] },
```

Next, we define the remaining section of the overriding plate that extends to the rightward edge of the model. This section is taken to be a uniform thickness, with an age of 50 Myr. We define it by using a ridge at a constant distance in the y coordinate away from the slice taken to be the model domain (2 in Figure A1)

```
{ "model":"oceanic plate", "name":"Slab Ridge", "max depth":150e3,"min depth":0,
  "coordinates":[[-500e3,-100e3],[-500e3,100e3],[2000e3,100e3],[2000e3,-100e3]],
  "temperature models":[
    {"model":"half space model",
     "min depth":0,  "max depth":150e3, "spreading velocity":0.05,
     "top temperature":273, "bottom temperature":-1,
     "ridge coordinates": [[[-1000e3,-100e3],[-1000e3,100e3]]] }] },
```

Following, we define the oceanic plate that will connect to the slab (3 in Figure A1). It is defined out of

the left model boundary with negative x coordinates, as to prevent melting and upwelling associated with

the ridge within the domain. The "spreading velocity" here needs to match the convergence velocity

prescribed in each respective model and the distance the ridge needs to be away from the slab must

correspond with the age defined at the trench.

```
{ "model":"subducting plate", "name":"Slab",
 "coordinates":[[2000e3,-100e3],[2000e3,100e3]],
 "dip point":[4500e3,0],
  "segments":[
  {"length":200e3, "thickness":[300e3], "top truncation":[-100e3], "angle":[0,30]},
  {"length":100e3, "thickness":[300e3], "top truncation":[-100e3], "angle":[30,50]}],
 "temperature models":[{"model":"mass conserving",
    "density":3300,"thermal conductivity":3.3,"adiabatic heating":true,
    "plate velocity":0.05,"ridge coordinates":[[[-1000e3,-100e3],[-1000e3,100e3]]],
    "coupling depth":100e3, "shallow dip":30.0, "taper distance":100e3,
    "min distance slab top":-100e3, "max distance slab top":200e3}]
 },
```

Then, we define the protoslab (4 in Figure A1). Like the previous feature, the "plate velocity" must match

the convergence velocity of the model and have the ridge coordinates match the "Slab Ridge".

```
{ "model":"subducting plate", "name":"weak zone",
 "coordinates":[[2000e3,-100e3],[2000e3,100e3]],
 "dip point":[4500e3,0],
  "segments":[
  {"length":200e3, "thickness":[10e3], "top truncation":[-10e3], "angle":[0,30]},
  {"length":100e3,  "thickness":[10e3], "top truncation":[-10e3], "angle":[30,50]}],
 "composition models":[
 {"model":"uniform", "compositions":[2], "min distance slab top":-20e3,
     "max distance slab top":0}]
   },
```

Finally, the last feature here creates the composition associated with the shear zone (composition 2). It

does this right above the "Slab" feature and has a thickness of 10 km.

```
{ "model": "mantle layer", "name": "mantle to subtract", "min depth":-10e3, "max depth":3000e3,
  "coordinates" :[[0,1000e3],[4500e3,1000e3],[4500e3,-100e3],[0,-100e3]],
  "temperature models":[{"model":"adiabatic", "min depth":-10e3, "max depth": 3000e3, "operation": "subtract"}]}
```

The final feature subtracts out the adiabat that worldbuilder creates. Then, the adiabat is added back in the ASPECT parameter file. This was done because it was thought that Worldbuilder and ASPECT calculated the adiabat in different ways. This turned out to be false, but for the models to run the way they are, this is necessary unless changes to the parameter file are made.

ASPECT Stage 1 Parameter file

We have two ASPECT parameter files for each model, one for each stage of the models (initiation of the protoslab, and then initiation of back-arc spreading). The parameter files themselves are well commented, so here we will go over some of the important choices made within the Stage 1 parameter file for the 50 Myr, 5 cm/yr convergence velocity model. The Stage 1 and Stage 2 parameter files are nearly identical, with a few key differences that we will also go over here.

```
1    # 2D model of the first stage of the back arc spreading model
2    # Stage 1 initializes the slab from a protoslab and does not
3    # yet induce the kinematic back arc spreading
4
5    set Dimension                          = 2
6    #Needs to be set to be the same as the .wb file
7    set Adiabatic surface temperature      = 1570 # K
8
9    # Because our model includes melt transport, it is nonlinear and we have to
10   # use an iterative solver scheme, that iterates between solving the temperature
11   # composition and Stokes equations.
12   set Nonlinear solver scheme            = iterated Advection and Stokes
13
14   # Needs to output to mpi-io folder
15   set Output directory                   = /group/billengrp-mpi-io/tjbrink/outputs/basc_models/50_5_original
16
17   # using a worldbuilder file to set initial/boundary temperature conditions
18   # and initial/boundary composition conditions
19   set World builder file                 = protoslab_basc_fix.wb
20
21   # The end time for stage 1 of the model. This is approximately the time it takes
22   # for the slab to pass the 660 km boundary.
23   # Note: this will be different for different convergence velocities
24   set End time                           =22e6 #yrs
25
26   # removing pressure normalization - otherwise ASPECT will set the surface pressure
27   # average to be 0, which due to our surface kinematics (very strong positive pressure at trench)
28   # leads to large negative pressures on most of the surface
29   set Pressure normalization = no
```

Here we set what worldbuilder file to use. In this case, we keep the worldbuilder file in the same location as the parameter file that we use to run it. Additionally, here we set the end time here for the Stage 1 parameter file, which needs to be the same as the start time of back-arc spreading in the Stage 2 parameter file.

```
31    ##################### Melting and freezing #######################
32
33    # Because the model includes reactions that might be on a faster time scale
34    # than the time step of the model (melting and the freezing of melt), we use
35    # the operator splitting scheme.
36    set Use operator splitting                = true
37
38    subsection Solver parameters
39      subsection Operator splitting parameters
40        # We choose the size of the reaction time step as 200 years, small enough
41        # so that it can accurately model melting and freezing
42        set Reaction time step                   = 2e2 # same as ASPECT MOR cookbook
43
44        # Additionally, we always want to do at least 10 operator splitting time
45        # steps in each model time step, to accurately compute the reactions.
46        set Reaction time steps per advection step = 10 # same as ASPECT MOR cookbook
47      end
48
49      # Because this model includes strong localized viscosity contrasts we
50      # increase the robustness of the solver at the cost of memory consumption.
51      subsection Stokes solver parameters
52        set GMRES solver restart length = 200
53      # increasing number of steps to allow convergence of increased model size
54        set Maximum number of expensive Stokes solver steps = 3000
55      end
56    end
```

When modeling melt in ASPECT, we need to turn on operator splitting in order to model the different timescales of melting/melt flow to mantle flow. Then, we choose two different parameters that control how this operator splitting is done. First is the

```
84    subsection Material model
85      set Model name = melt simple
86      subsection Melt simple
87        set Reference permeability                = 1e-7 #m^2
88        set Melt extraction depth                 = 0.0 #m
89        set Freezing rate                         = 0.005 #1/yr
90        set Melting time scale for operator splitting = 2e2 #yr
91        set Exponential melt weakening factor     = 20 # dimensionless
92        set Thermal expansion coefficient         = 3e-5 #1/K
93
94        set Solid compressibility                 = 4.2e-12 # 1/Pa
95
96        # variables for viscosity model
97        # calibrated for the slab to have a viscosity of 1e23 Pa*s at the surface,
98        # ~1e20 in the upper mantle, and ~1e22 at the top of the lower mantle
99        set Thermal viscosity exponent = 10
100       set Reference shear viscosity  = 1e18
101
102       # uncomment the below to 'turn' off melting
103       # This works by increasing the solidi and liquidi in the quadratic
104       # Katz parameterezations to over 10000 K
105       #set A1 = 10000 # C
106       #set B1 = 10000 # C
107       #set C1 = 10000 # C
108     end
109   end
```

Here is where constant material parameters are defined. Most values here apart from the variables for the

shear viscosity model are taken from the MOR cookbook. In the future it is likely worth testing different

values of freezing rate to see how that affects the melt region and enriched crust. Note that melting can be

turned 'off' by increasing A1, B1, and C1 to a large value.

```
111   #################### Model geometry #######################
112
113   # Model has dimension os 4500 km wide and 3000 km deep
114   # wide enough for center to be far from edge effects and deep enough to approximate CMB
115   subsection Geometry model
116     set Model name = box
117
118     subsection Box
119       set X extent      = 4500e3 # m
120       set Y extent      = 3000e3 # m
121
122       # To keep the aspect ratio of our elements close to one, we chose the
123       # coarse mesh is such a way that it has more elements in X than in Y the
124       # direction, in the same ratio as the aspect ratio of the model.
125       set X repetitions = 3
126       set Y repetitions = 2
127     end
128   end
```

This section defines the model domain and large scale geometry of the mesh. The depth of the model is

set to 3000 km in order to maintain a 3:2 aspect ratio, which is set using the "set X repetitions = 3" and

"set Y repetitions = 2".

```
138   ##################### Velocity #######################
139   # Top layer has a prescribed surface traction that will be applied in two stages
140   # The first stage will have a rightward convergence velocity on the subducting plate
141   # that smoothly transitions to 0 at the trench.
142   # The second will keep that convergence velocity and initiate a BASC that moves away from the arc
143   # at 1/2 the BASC velocity
144   subsection Boundary velocity model
145     set Prescribed velocity boundary indicators = top:function
146     # bottom of the model has
147     set Tangential velocity boundary indicators = bottom
148     subsection Function
149       # We choose a convergence rate of vsub, trench location xtr=2000 km, and width of velocity transtion
150       # xwt = 50 km.
151       set Function constants  = vsub = 0.05 , xtr=2000e3 , xwt =50e3
152       set Variable names      = x,z
153
154       set Function expression = (x<=xtr ? vsub : \
155         (((x>=xtr) && (x<=xtr+xwt)) ? vsub-vsub*(3*((x-xtr)/xwt)^2-2*((x-xtr)/xwt)^3) : 0 ) ) ; 0
156   #if(x<x0,(1-(x/x0-1)*(x/x0-1))*u0,u0); 0
157     end
158   end
```

Here is where we prescribe the surface and bottom boundary conditions. The top is prescribed using a

function in a set of if-then statements that prescribe different boundary conditions in different regions on

the surface. Here there 3 different regions on the surface. The constant convergence rate applied to the

slab plate, the 0 velocity applied to the overriding plate, and a smooth transition between the two using a

smooth-step function (so there are no discontinuities).

```
160   # We prescribe the lithostatic pressure as a boundary traction on
161   # the left and right side of the model, so that material can flow in and out
162   # according to the flow induced by the moving plates/slab.
163   subsection Boundary traction model
164
165
166     set Prescribed traction boundary indicators = right:initial lithostatic pressure, left:initial lithostatic pressure
167
168     subsection Initial lithostatic pressure
169       # We calculate the pressure profile at the right model boundary.
170       set Representative point        = 4500e3, 3000e3 # m
171       set Number of integration points = 3000 # default is 1000, not enough for larger domain
172     end
173   end
```

This section applies the stress free boundary conditions to the left and right boundaries of the model. This

allows for material to flow in and out. The "Representative point" is where the pressure profile for the

side boundaries is calculated.

```
175  ##################### Temperature #######################
176
177  # set this subsection to add in ASPECTs adiabatic heating model -required to avoid using WBs adiabatic model
178  # This requires subtracting out worldbuilders adiabat in the .wb file
179  subsection Initial temperature model
180    set List of model names = world builder, adiabatic
181    set List of model operators = add
182    subsection Adiabatic
183      subsection Function
184        set Function expression = 0;0;0 #number of 0's is the number of compositional fields
185      end
186    end
187  end
188
189  # We choose a constant temperature at the top and bottom of the domain
190  # and we choose a potential temperature of 1570 K (1300 °C).
191  # Note this value is from the original MOR cookbook
192
193  subsection Boundary temperature model
194    set Fixed temperature boundary indicators = top, bottom, left, right
195    set List of model names = initial temperature
196  end
197
198  # We want to include latent heat of melting and freezing in the model, as it is
199  # an essential process for the temperature evolution. We also include adiabatic heating.
200  # the adiabatic heating model is also required in order to add back in the temperature subtracted from WB
201  subsection Heating model
202    set List of model names = latent heat, adiabatic heating
203  end
204
205  # Melt moves with a different velocity than the solid, and transports energy,
206  # so we include this process in the model.
207  subsection Melt settings
208    # We want to solve the McKenzie Equations to track the flow of melt.
209    set Include melt transport = true
210    set Heat advection by melt = true
211  end
```

This section of the parameter file handles how we deal with temperature. First here, we add back in ASPECTs adiabatic heating model, as we subtracted Worldbuilder's heating model. Additionally, all side temperature boundary conditions are taken to the initial temperature. And because we want to include the latent heat of melt/crystallization, we need add that as a heating model (same for adiabatic heating). Additionally, we need to modify "Melt settings" and turn on melt transport and melt heat advection.

```
213  ##################### Composition #######################
214
215  # We need three compositional fields: The porosity field to track the motion of
216  # melt, the peridotite field to track the depletion of material, which is
217  # changed by the melting and freezing reactions, and shear_zone to create the
218  # weak layer needed to induce subduction.
219  subsection Compositional fields
220    set Number of fields = 3
221    set Names of fields = porosity, peridotite, shear_zone
222    # setting shear zone to not be advected like the other fields
223    set Compositional field methods = field, field, static
224  end
225
226  # Use the worldbuilder file for initial composition
227  subsection Initial composition model
228    set Model name = world builder
229  end
230
231  # The boundary conditions (which are relevant for material inflowing at the
232  # side boundary of the model) are the same as the initial conditions.
233  subsection Boundary composition model
234    set Fixed composition boundary indicators   = top, bottom, right, left
235    set List of model names = initial composition
236  end
```

There are three compositional fields within these models. The first is porosity, which tracks melt. Next is

peridotite, which tracks the depletion/enrichment. And finally, there is the static (it cannot advect)

shear_zone, which we use define the shear zone. Then, we get the initial composition model from

worldbuilder, including the location of the shear_zone composition. Additionally, we apply composition

boundary conditions here that have the same uniform composition as the rest of the model.

```
238    ##################### Mesh refinement #########################
239
240    # The mesh has 5 different refinement levels, from most refined to least:
241    #    1. The shear zone, which is manuall
242    subsection Mesh refinement
243      #set Coarsening fraction                = 0.5
244      #set Refinement fraction                = 0.5
245
246      # A refinement level of 5 (4 global + 1 adaptive refinements) corresponds to
247      # a cell size of approximately 1 km.
248      set Initial adaptive refinement        = 5
249      set Initial global refinement          = 5
250      set Strategy                           = minimum refinement function, maximum refinement function, composition threshold
251      set Time steps between mesh refinement = 0
252
253      subsection Maximum refinement function
254        set Coordinate system  = cartesian
255        set Variable names     = x,y
256        set Function constants = x_width = 4500e3, y_depth = 3000e3, y1 = 100e3, y2 = 660e3, box_width = 800e3, box_depth = 150e3
257        set Function expression = ((x>(x_width-box_width)/2) && (x<(x_width+box_width)/2) && (y>y_depth-box_depth) ? 9 : \
258                                  ( ((x<=(x_width-box_width)/2) || (x>=(x_width+box_width)/2)) && (y>y_depth-y1) ? 8 : \
259                                  ( ((x<=(x_width-box_width)/2) || (x>=(x_width+box_width)/2)) && ((y<=y_depth-y1) && (y>y_depth-box_depth)) ? 7 : \
260                                  ( (y<=y_depth-box_depth && y>y_depth-y2) ? 7 : \
261                                  ( (y<=y_depth-y2) ? 5 : 5) ) ) ) )
262      end
263
264      subsection Minimum refinement function
265        set Coordinate system  = cartesian
266        set Variable names     = x,y
267        set Function constants = x_width = 4500e3, y_depth = 3000e3, y1 = 100e3, y2 = 660e3, box_width = 800e3, box_depth = 150e3
268        set Function expression = ((x>(x_width-box_width)/2) && (x<(x_width+box_width)/2) && (y>y_depth-box_depth) ? 9 : \
269                                  ( ((x<=(x_width-box_width)/2) || (x>=(x_width+box_width)/2)) && (y>y_depth-y1) ? 8 : \
270                                  ( ((x<=(x_width-box_width)/2) || (x>=(x_width+box_width)/2)) && ((y<=y_depth-y1) && (y>y_depth-box_depth)) ? 7 : \
271                                  ( (y<=y_depth-box_depth && y>y_depth-y2) ? 7 : \
272                                  ( (y<=y_depth-y2) ? 5 : 5) ) ) ) )
273
274
275      end
276
277      # Refines where shear_zone is > 0.5 (its value is 1 in the .wb file)
278      # I don't know why, but it is not currently refining on the porosity field...
279      # could be because the maximum and minimum refinement functions are overriding it?
280      subsection Composition threshold
281        set Compositional field thresholds = 1e-6, 1.0, 0.5
282      end
283    end
```

This section handles the mesh refinement. We have an initial adaptive refinement of 5 (leads to cell sizes

of ~23 km), and an adaptive refinement of 5 (leads to cell sizes of ~0.7 km at full refinement). The

minimum and maximum refinement functions coarsen and refine the mesh as shown in Figure 4 and have

the same syntax as the surface velocity function – using if-then statements to refine the mesh in certain

regions. Additionally, we use a compositional threshold to refine the shear_zone composition. The order

of the numbers in "set Compositional field thresholds = 1e-6, 1.0, 0.5" is the same order as they are

defined in the Compositional fields subsection in the previous code block.

```
285    #################### Postprocessing ########################
286
287    subsection Postprocess
288
289      set List of postprocessors = visualization, composition statistics, velocity statistics
290
291      # We mainly want to look at material properties of the solid and the melt.
292      subsection Visualization
293        set List of output variables    = material properties, melt material properties, melt fraction
294        # set Number of grouped files    = 0
295        subsection Material properties
296          set List of material properties = density, viscosity
297        end
298
299        # To see in which cells melt transport is modelled, it can be useful to look
300        # at the property 'is melt cell', so we include it in the output. In addition,
301        # we always visualize the compaction pressure 'p_c' if this postprocessor is
302        # used.
303        subsection Melt material properties
304          set List of properties = compaction viscosity, permeability, fluid density, is melt cell
305        end
306
307        set Time between graphical output = .05e6
308      end
309
310    end
311
312    # We write a checkpoint every 30 time steps, so that we are able to restart
313    # the computation from that point.
314    subsection Checkpointing
315      set Steps between checkpoint = 30
316    end
```

And finally, here is the postprocessing subsection, where we decide what model parameters to output and how often to output. Additionally, we use checkpointing in order to restart with a different parameter file.

ASPECT Stage 2 Parameter file

Here I will go over the main differences between the two parameter files. For the most part, everything here needs to be identical to the Stage 1 parameter file, but with a few key differences that allow the model to pick up running again and to initiate back-arc spreading.

```
13    # Needs to output to mpi-io folder
14    set Output directory                         = /group/billengrp-mpi-io/tjbrink/outputs/basc_models/50_5_5
15
16    # Need to start from checkpoint created in Stage 1
17    set Resume computation                       = true
```

First we need to make sure the output directory is the same as the Stage 1 parameter file, and then we need to set "Resume computation" to true so that it picks up where Stage 1 left off. This only works if checkpointing is enabled in Stage 1.

```
140    #################### Velocity #########################
141    # Top layer has a prescribed surface traction that will be applied in two stages
142    # The first stage will have a rightward convergence velocity on the subducting plate
143    # that smoothly transitions to 0 at the trench.
144    # The second will keep that convergence velocity and initiate a BASC that moves away from the arc
145    # at 1/2 the BASC velocity
146    subsection Boundary velocity model
147      set Prescribed velocity boundary indicators = top:function
148      # bottom of the model has
149      set Tangential velocity boundary indicators = bottom
150      subsection Function
151        # xtr is trench location, xba is back arc start location, xwt is the width of the vel transition at the trench,
152        # xwba is the width of the velocity transition at the back arc,  vsub is convergence rate, vbasc is
153        # the back arc spreading rate, and t0 is the start time of stage 2.
154        set Function constants = xtr = 2000e3, xba=2275e3, xwt = 50e3, xwba=50e3, vsub=0.05, vbasc = 0.05, t0 = 22e6
155        set Variable names      = x,z,t
156
157        set Function expression = (x<=xtr ? vsub : \
158               (((x>=xtr) && (x<=xtr+xwt)) ? vsub-vsub*(3*((x-xtr)/xwt)^2-2*((x-xtr)/xwt)^3) : \
159               (((x>xtr+xwt) && (x<=xba-0.5*xwba+0.5*vbasc*(t-t0))) ? 0 :\
160               (((x>xba-0.5*xwba+0.5*vbasc*(t-t0)) && (x<=xba+0.5*xwba+0.5*vbasc*(t-t0))) ? \
161               vbasc*(3*((x-(xba+0.5*vbasc*(t-t0)-0.5*xwba))/xwba)^2-2*((x-(xba+0.5*vbasc*(t-t0)-0.5*xwba))/xwba)^3): \
162               vbasc) ) ) ) ; 0
163      end
164    end
```

The other main difference is the surface velocity boundary conditions. In total, there are 5 separate surface velocity conditions applied. Similarly to the Stage 1 parameter file, we have a convergence velocity applied to the slab plate and an arc region held at a fixed velocity, with a transitional region between them. Then we also have back-arc spreading as a rightward (positive x direction) velocity. The boundary between the fixed arc region and rightward back-arc spreading also migrates right at half the back-arc spreading velocity, still with a smooth transitional region between the two regions.

Changes to the Melt simple Material Model

In order incorporate our own changes to the viscosity formulation, edits to the Melt simple material model were made. The broad changes are outlined in the methods section, but here we will go over changes to the code. Melt simple is saved as melt_simple.cc in the ASPECT source in the directory material_models.

```
230          // MIB: create a flag that gets set for each node indicating if node is in the shear zone
231          bool in_shear_zone = false;
232
233          // MIB: if in the lower mantle multiple viscosity by constant factor to get viscosity jump
234          double top_lower_mantle_depth = 660e3; // m
```

This is the first change made, we add a boolean in_shear_zone that tracks whether a node is in the shear zone. Here we also define the depth of the top of the lower mantle.

```
241            if (this->include_melt_transport())
242              {
243                const unsigned int porosity_idx = this->introspection().compositional_index_for_name("porosity");
244                const unsigned int peridotite_idx = this->introspection().compositional_index_for_name("peridotite");
245                // MIB create a idx for shear zone
246                const unsigned int shear_zone_idx = this->introspection().compositional_index_for_name("shear_zone");
```

Here is where we define the shear_zone as its own compositional field, allowing for us to use it as a

compositional field within the ASPECT parameter file.

```
314                for (unsigned int c=0; c<in.composition[i].size(); ++c)
315                  {
316                  // MIB turn on a flag that indicates this node is part of the shear zone
317                  if (in.composition[i][shear_zone_idx] == 1)
318                    {
319                      in_shear_zone = true;
320                    }
321                  // fill reaction rate outputs
```

Then here, we add an if statement that checks if the shear_zone composition is equal to 1, and if so set the

in_shear_zone flag to true

```
368            if (this->include_adiabatic_heating ())
369              {
370                const double T_offset = 450; // TJB adding in offset temperature to shift viscosity to more acceptable range
371                const double delta_temp = in.temperature[i]-this->get_adiabatic_conditions().temperature(in.position[i]) - T_offset;
372            //increasing max range from 1e4 to 1e5
373                visc_temperature_dependence = std::max(std::min(std::exp(-thermal_viscosity_exponent*delta_temp/ \
374                (this->get_adiabatic_conditions().temperature(in.position[i])-T_offset)),1e5),1e-4);
375              }
```

The next change is within an if statement that checks if adiabatic heating is turned on, which in our

models it always is. We add the T_offset (same as T_{offset} in the methods) and subtract that from

delta_temp. Additionally, we increase the maximum range of the visc_temperature_dependence to 1e5, as

before it was 1e4. These together, result in a higher viscosity everywhere in the model and a greater upper

limit on viscosity.

```
386          // TJB, adding in depth dependent viscosity factor here for upper mantle -above 660 km
387          // Without this section, viscosity will decrease with depth and lead to rapid convection
388          double visc_depth_dependence = 1;
389          const double depth_mag_UM = 10; // value maximum multiplier for upper mantle
390          // TJB, these values came from setting the viscosity of the top of the lower mantle to 1e22 Pa*s and the bottom to 3e22.
391          const double depth_mag_top_LM = 390; // value for multiplier at top of lower mantle
392          const double depth_mag_bottom_LM = 5700; // value for multiplier at bottom of lower mantle
393            const double model_bottom = 3000e3; // m
394          if (this->get_geometry_model().depth(in.position[i])<top_lower_mantle_depth)
395              {
396                double visc_depth_dependence1 = std::min((depth_mag_UM*this->get_geometry_model().depth(in.position[i])/top_lower_mantle_depth),depth_mag_UM);
397                visc_depth_dependence = std::max((visc_depth_dependence1),1.0);
398              }
399          else if ( this->get_geometry_model().depth(in.position[i])>top_lower_mantle_depth)
400              {
401                // TJB - this is a linear equation from the top to the bottom of the lower mantle - calculated from values above
402                visc_depth_dependence = (depth_mag_bottom_LM - depth_mag_top_LM)/(model_bottom - top_lower_mantle_depth) * \
403                (this->get_geometry_model().depth(in.position[i])) + (depth_mag_top_LM - ((depth_mag_bottom_LM - depth_mag_top_LM) \
404                /(model_bottom - top_lower_mantle_depth))*top_lower_mantle_depth);
405              }
```

This next section is where we calculate the depth viscosity factor θ_d as in equation 9. Lines 394-398

calculate this for the upper mantle (above 660 km), and lines 399-405 calculate this for the lower mantle

(below 660 km). The visc_depth_dependence increases linearly with depth from 0 to 10 in the upper

mantle, but has a minimum value of 1, meaning that the visc_depth_dependence will be 1 below 66 km

34

depth. The viscosity jump at 660 km is accommodated by the depth_mag_top_LM being set to 390, an increase by a factor of 39 relative to the bottom of the upper mantle. This then linearly increases in depth to 5700 (depth_mag_bottom_LM).

```
406    // TJB: Multiply viscosity by all new factors added in from above - viscosity T dependence, viscocity depth dependence,
407    // and depth viscosity factor
408    out.viscosities[i] *= visc_temperature_dependence *visc_depth_dependence;
409
410        // std::cout << ",final visc: " << out.viscosities[i] << "\n";
411    // MIB: assign fixed viscosity to the shear zone: supersedes everything above.
412    // TJB: Note this value should be set to be about the same viscosity of the mantle wedge
413    double shear_zone_viscosity = 1e20; // Pa s
414
415    if (in_shear_zone == true)
416        {
417        out.viscosities[i] = shear_zone_viscosity;
418        in_shear_zone = false; // TJB: Reset Flag to false
419        }
```

And finally, here is where we multiply both the modified visc_temperature_dependence and visc_depth_dependence by the previously calculated porosity dependent viscosity. And then, we override this calculation wherever in_shear_zone is true and set the viscosity to 1e20.

Figures
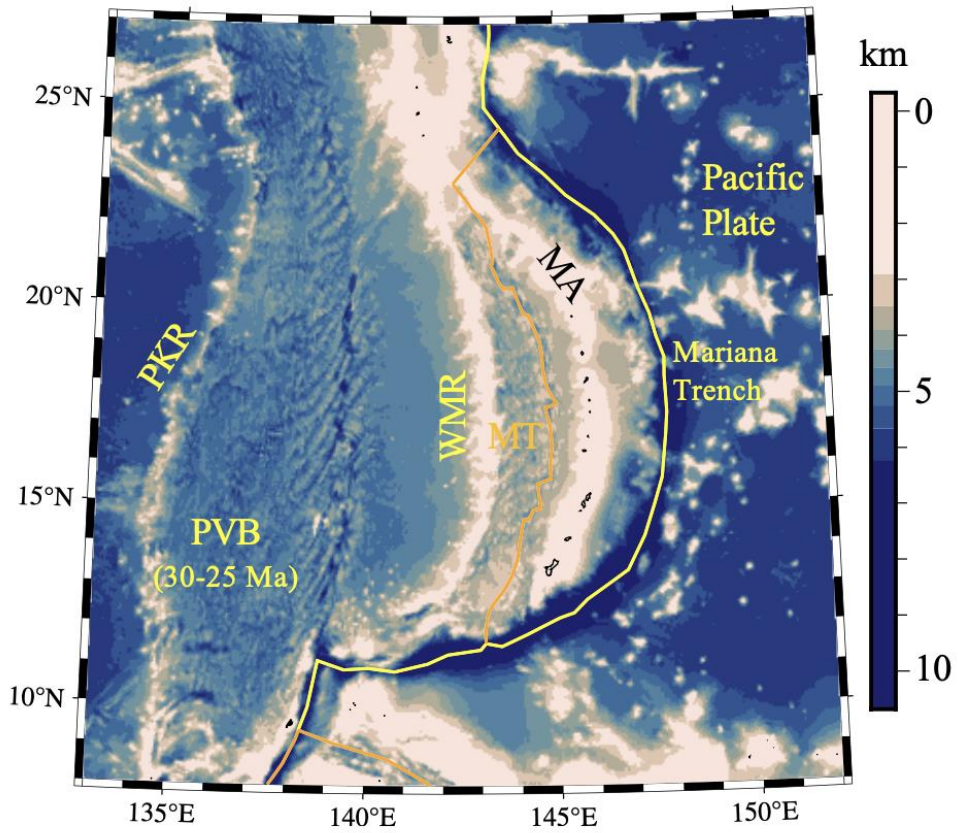
Figure 1) Bathymetric maps of the Mariana subduction zone illustrating features resulting from two episodes of back-arc spreading. PKR: Palau-Kyushu Ridge; PVR: Parece Vela Basin.; WMR: West Mariana Ridge; MA: Mariana Arc (active); MT: Mariana Trough (active BASC).
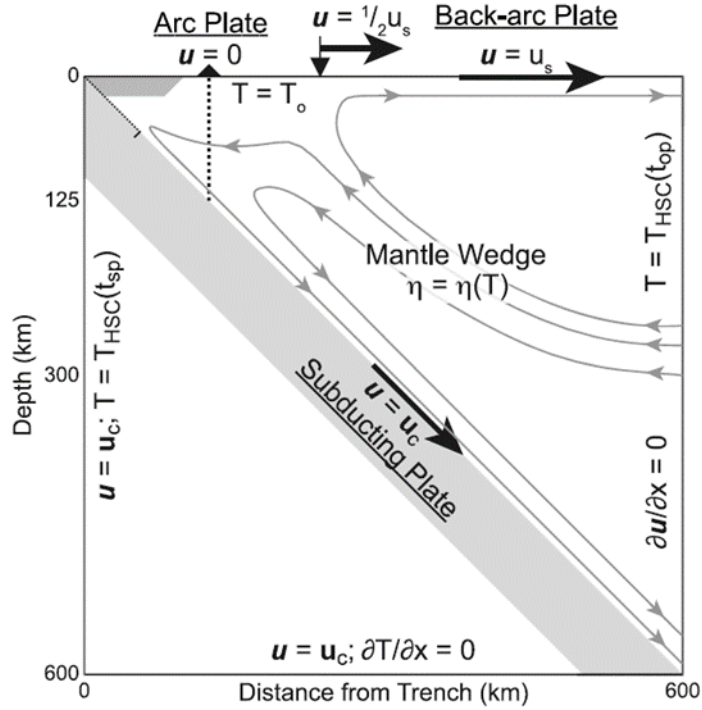
Figure 2) The kinematic model set up from Hall et al. (2012) to set up back-arc spreading with a total spreading rate of $\mathbf{u}_s$, migrating away from the Arc Plate at ½ $\mathbf{u}_s$ with an accompanying subducting slab sinking at a rate $\mathbf{u}_c$
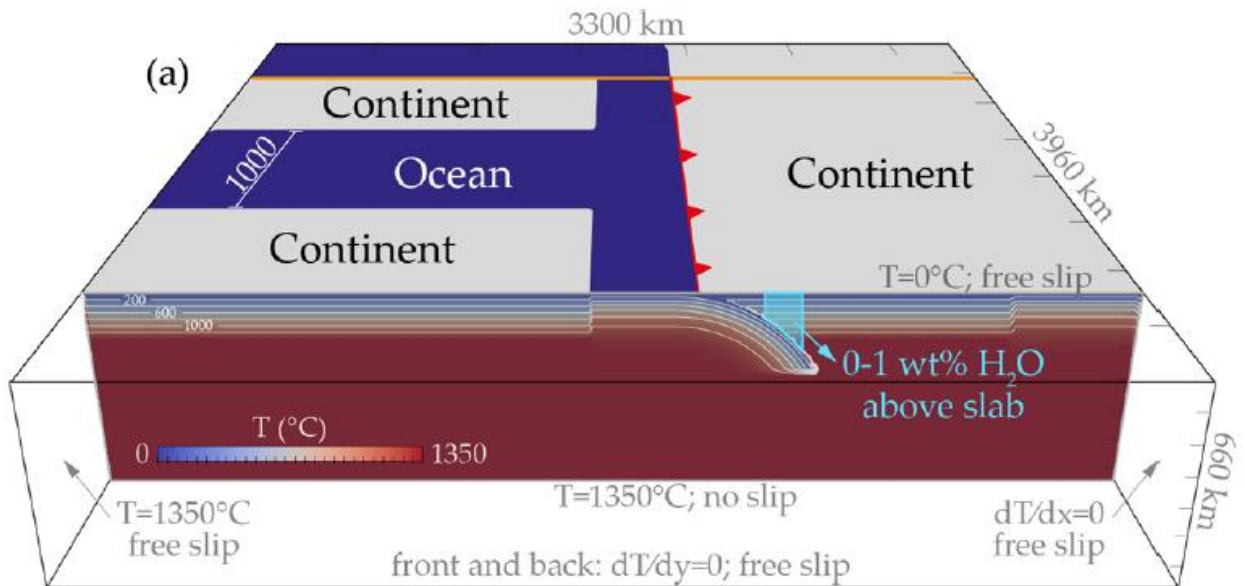
Figure 3) The dynamic 3D model set up from Magni (2019). The configuration of the lower-density continental plates create a continental collision and subsequent rapid trench rollback within the subduction oceanic plate. Thus, creating a back-arc spreading center.
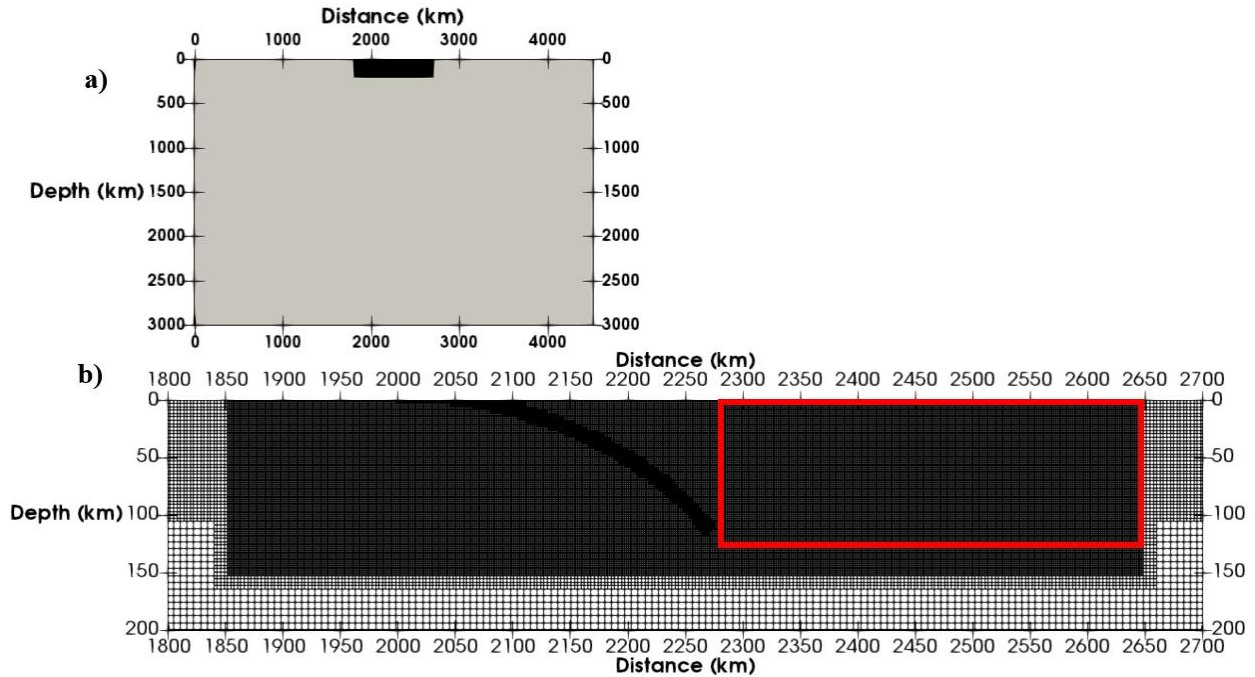
Figure 4) a: The entire Model domain and has dimensions 4500 km by 3000 km. The black box represents the region shown in b. The large model domain is used to mitigate the edge effects. b: Model mesh near the trench. The finest mesh in the model is in the shear zone and is ~0.7 km. Region of expected melt formation is outlined in the red box. Above which the surface velocity is applied in Stage 2 to initiate back-arc spreading.

a) Phase 1: Setting up slab from proto-slab

$u = \boldsymbol{u}_c$ $T = T_0$ No Slip

Immobile Shear zone   Proto-slab

3000km   Stress Free, T=T(z)   Stress Free, T=T(z)   660 km

Free Slip $T = T_{CMB}$

4500 km

b) Phase 2: Imposed back-arc spreading

$T = T_0$

Back-arc spreading center

$u = \boldsymbol{u}_c$ $u = 0$ $u = {}^1\!/_2\,\boldsymbol{u}_b$ $u = \boldsymbol{u}_b$

Immobile Shear zone

Dynamically generated slab from Phase 1

3000km   Stress Free, T=T(z)   Stress Free, T=T(z)   660 km

Free Slip $T = T_{CMB}$

4500 km
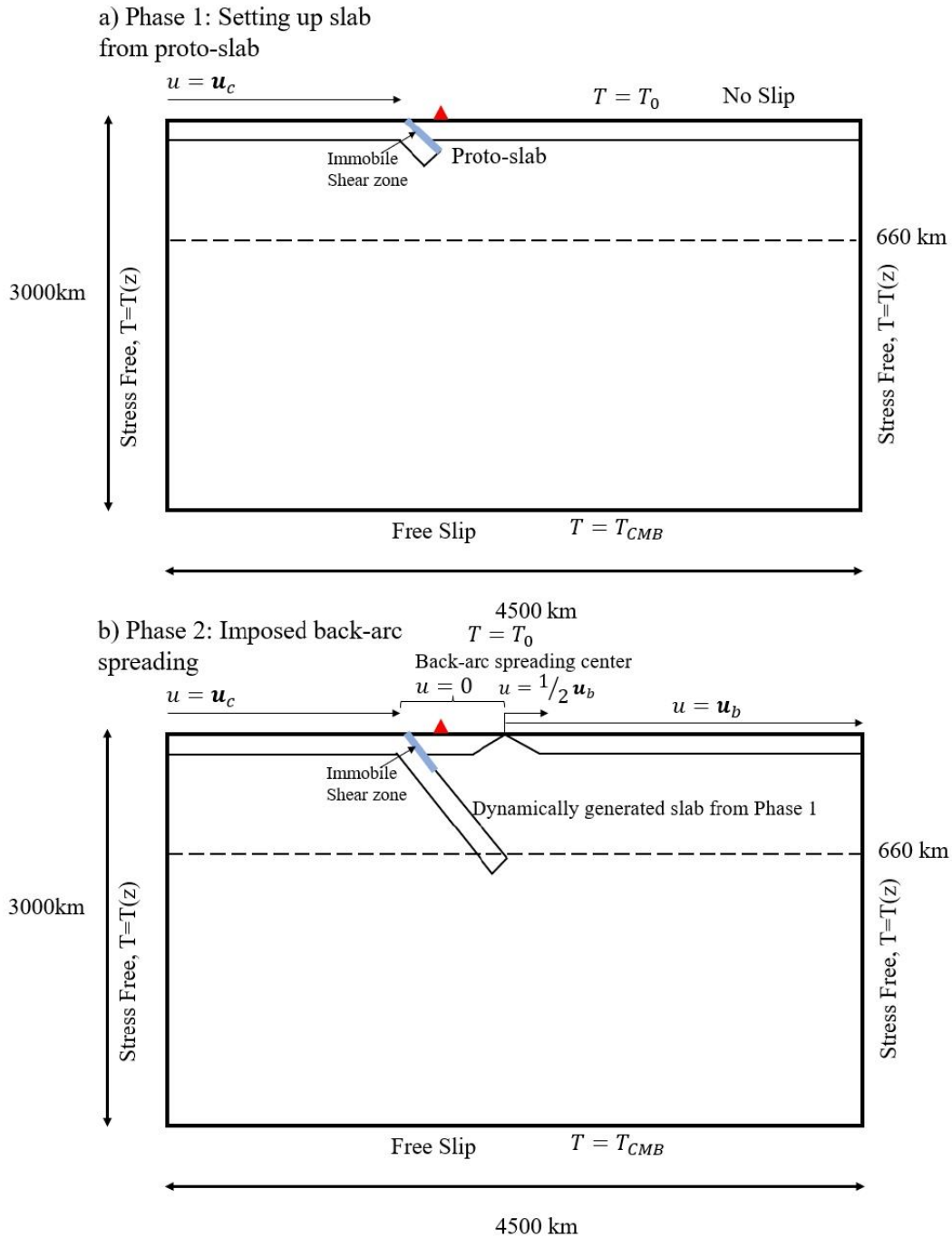
Figure 5) Schematic model set up. a) The first phase of the model starts with a protoslab and runs the model forward dynamically for each set of kinematic conditions to create a starting point for phase 2. b) In the second phase, back-arc spreading initiates.
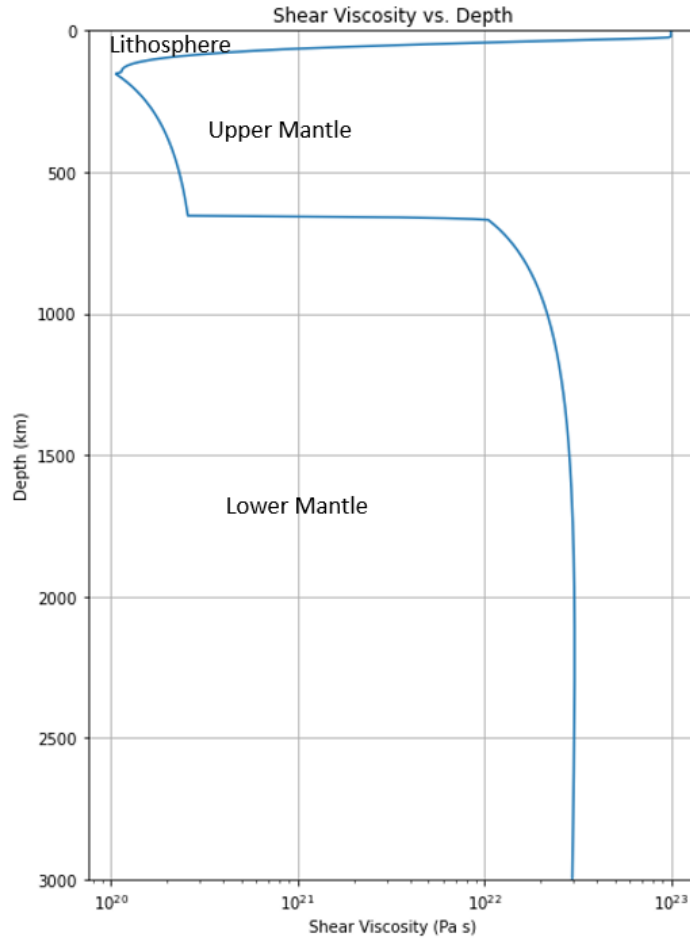
Figure 6) Shear viscosity versus depth from the surface to the base of the model domain. The viscosity cap at the surface is 1e23 Pa s and can be seen in the overlying plate in this example.
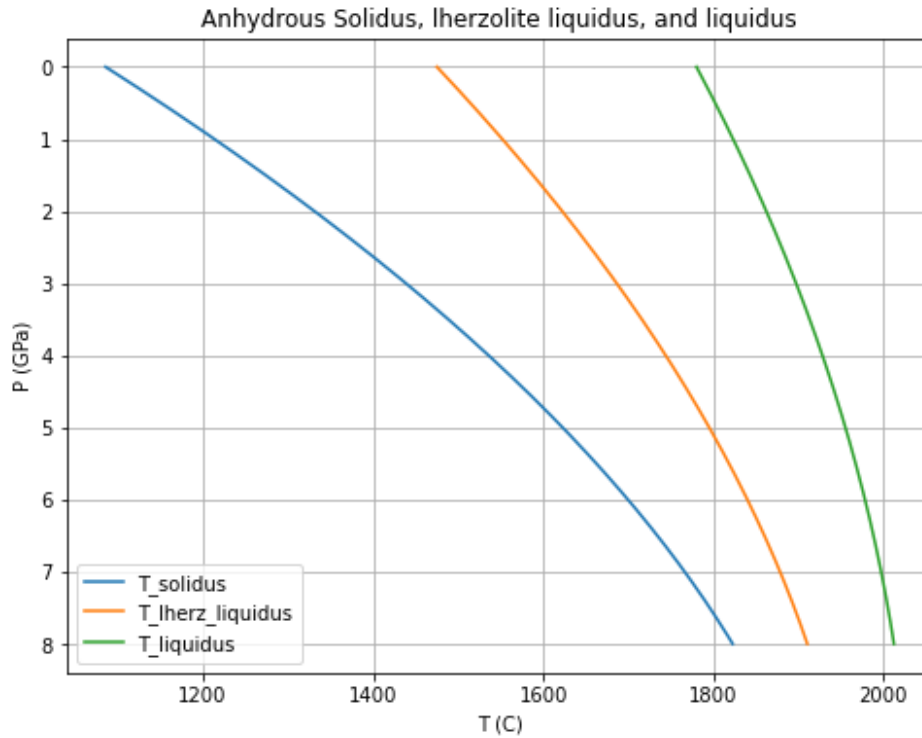
Figure 7) Solidus, lherzolite liquidus, and true liquidus for anhydrous conditions used in models using the

Katz et al., (2003) parameterization.
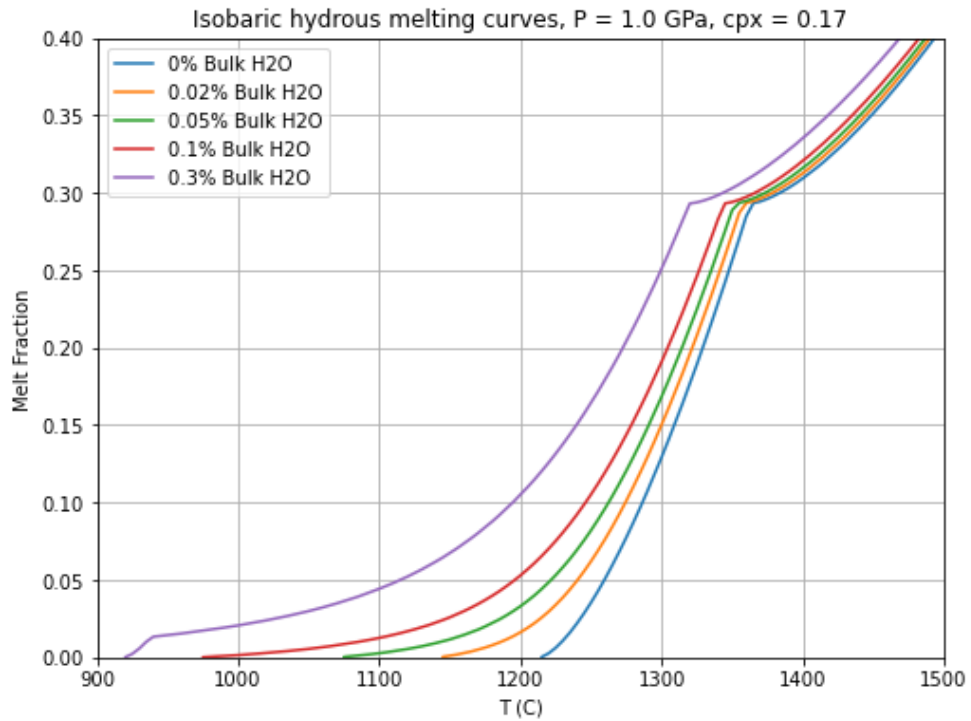
Figure 8) Melting curves calculated from the Katz et al. (2003) melting parameterization at 1 GPa for a composition of 83% olivine and 17% pyroxene. There is a significant drop in temperature required for melting with the addition of water, especially for low melt fractions. The sudden change in curvature for each curve at ~30% melt fraction is due to the complete melting of pyroxene. The sudden kink at low temperatures in the 0.3% Bulk H2O curve is due to reaching the water saturation limit.
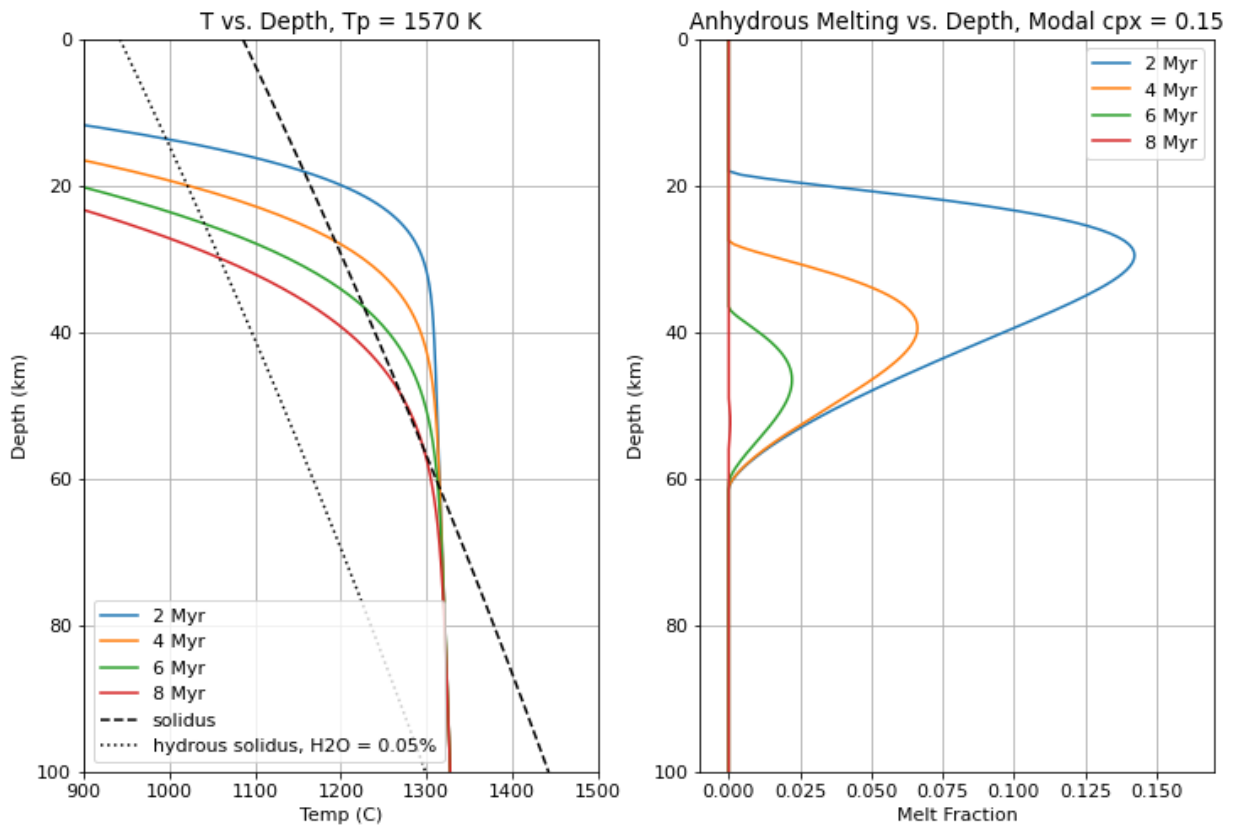
Figure 9) Left: Half-space cooling model temperature with adiabat plotted versus depth for a mantle potential temperature of 1570 K for various plate ages. The black dashed line shows the anhydrous solidus, and the black dotted line shows the hydrous solidus with a bulk water content of 0.05%. Melt fraction corresponds to how far beyond the solidus the temperature is. Right: The Anhydrous melt

fraction is plotted versus depth for the different plate ages. As the plate cools, the region of maximum

melt deepens as well.

No slab, u_b=5 cm/yr, A = 50 Myr, Model 2
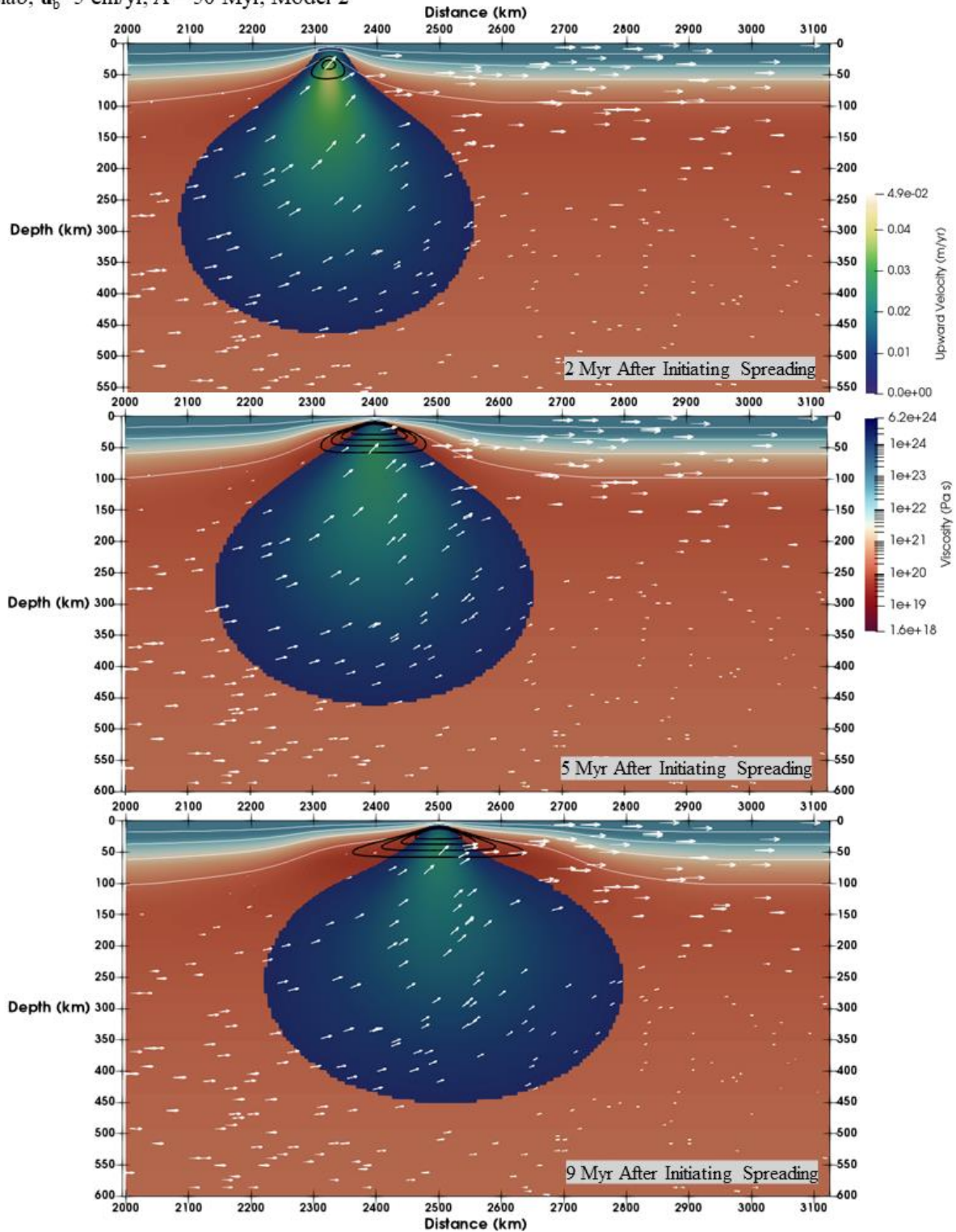
Figure 10) Evolution of upwelling in the MOR-style model. Upwelling region is defined by anywhere with an upward component of velocity greater than 0.5 cm/yr. The white contours are temperature contours starting at 300 °C to 1200 °C in 300 °C increments. The thicker black contours are melt contours starting at 1% melt fraction to 10% melt fraction in 3% increments. White arrows are the solid velocity field. The darker color plot shows the upwelling region. The upwelling region is large and diffuse, without being constrained by the presence of a slab. The upwelling and melt region and is also symmetric about the spreading axis.
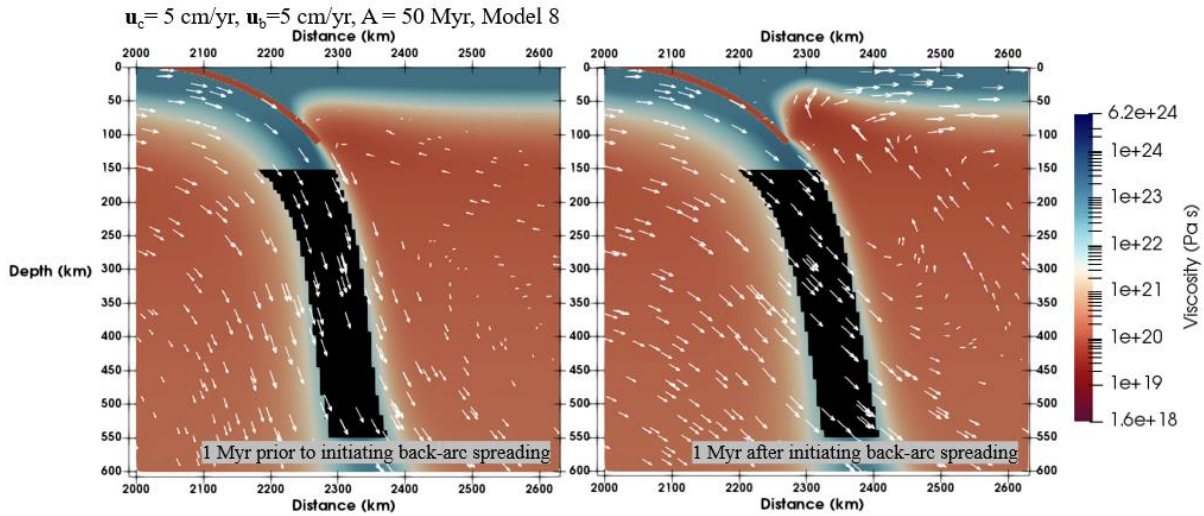
Figure 11) Velocity in the slab before and after initiating back-arc spreading in Model 10. The black region is the region sampled to calculate angle of sinking in the slab. The slab is differentiated from the mantle using the 1300 °C temperature contour as a boundary. Immediately following back-arc spreading, the velocity both inside and outside of the slab change.
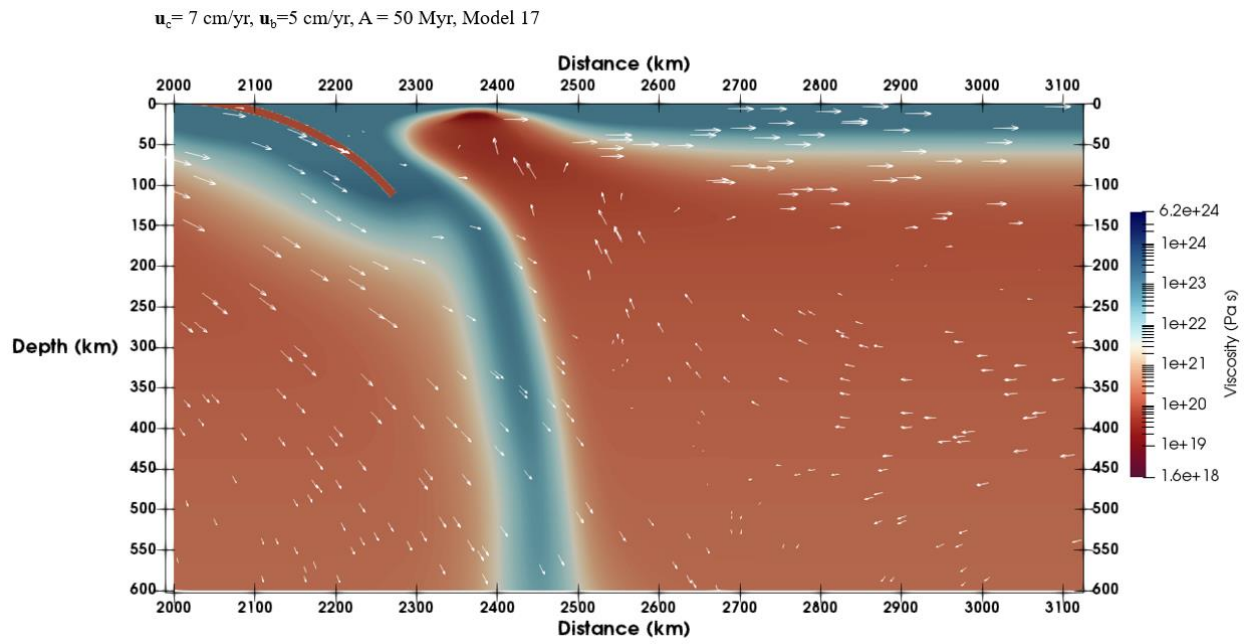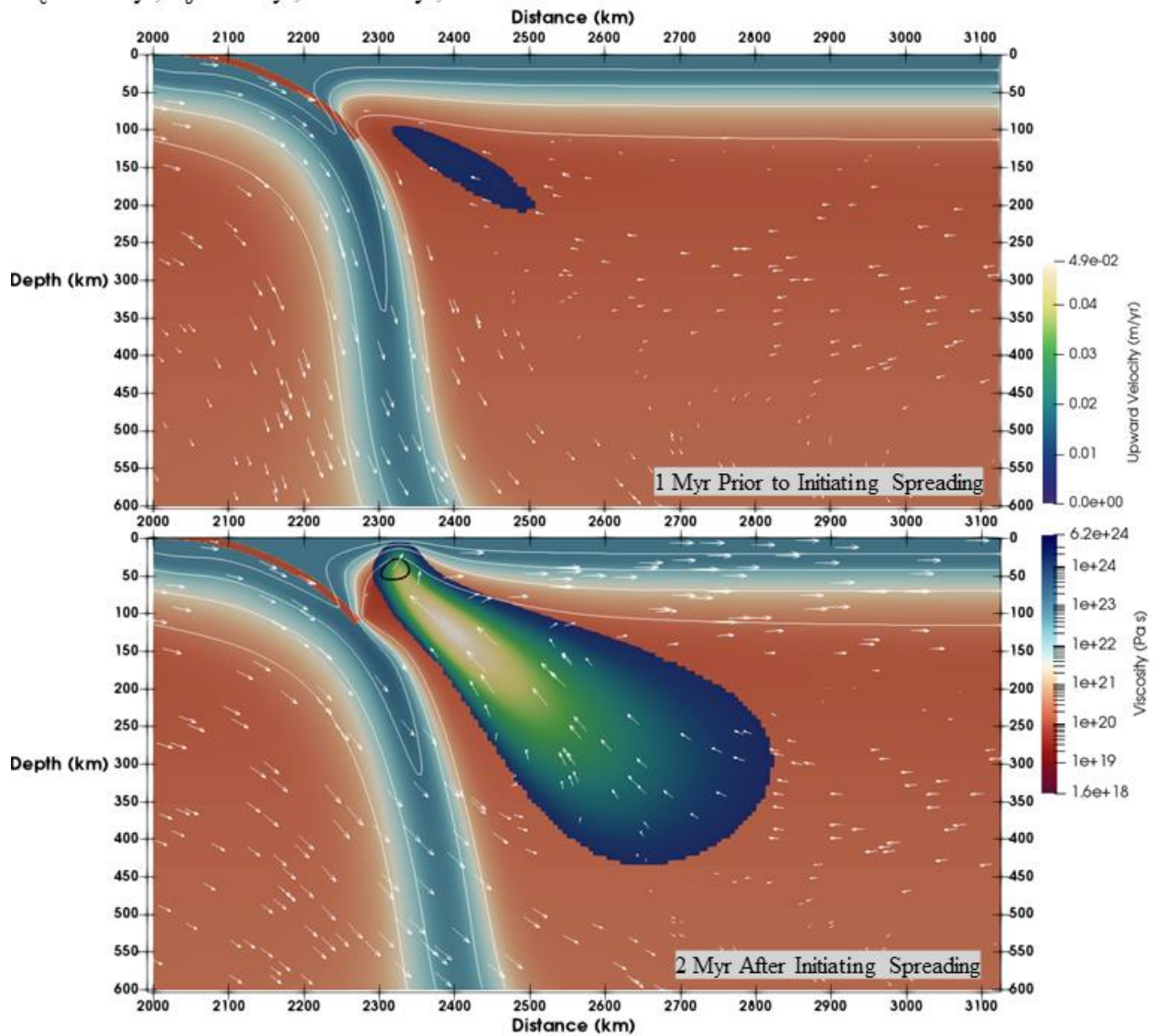
u_c= 7 cm/yr, u_b=5 cm/yr, A = 50 Myr, Model 17

Figure 12) An example of a faster convergence model passing through the shear zone. All Models 11 through 31 had this behavior.

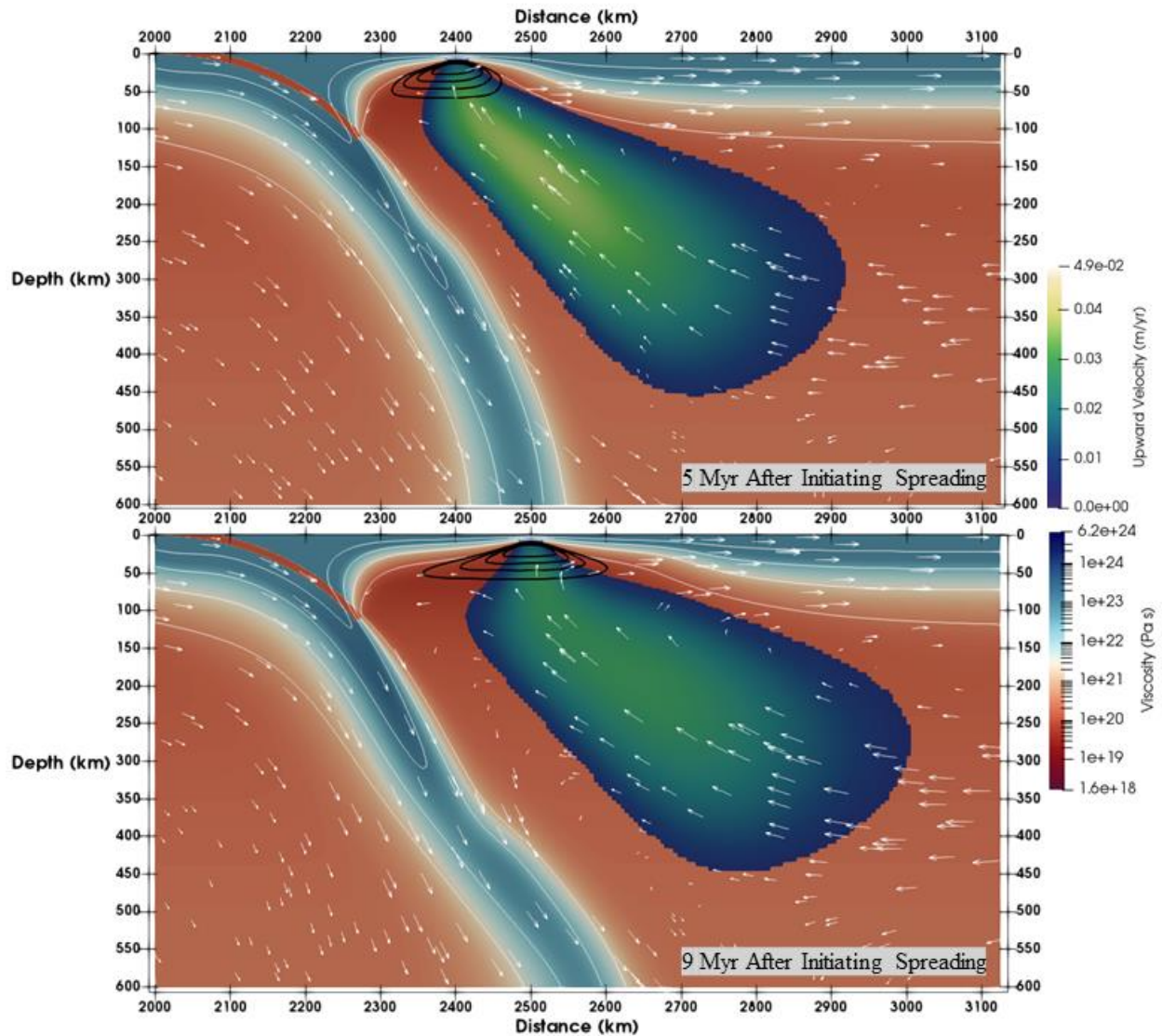u_c= 5 cm/yr, u_b=5 cm/yr, A = 50 Myr, Model 8

46

Figure 13) Evolution of upwelling region and melt region through time. The upwelling region is defined by anywhere with an upward component of velocity greater than 0.5 cm/yr. The white contours are temperature contours starting at 300 °C to 1200 °C in 300 °C increments. The thicker black contours are melt contours starting at 1% melt fraction to 10% melt fraction in 3% increments. White arrows are the solid velocity field. The top color plot shows the upwelling region. Before back-arc spreading, the upwelling region is small and has a small velocity. Immediately following back-arc spreading, the upwelling region rapidly grows and increases in velocity. Over the course of back-arc spreading, this

region expands and in doing so, the velocity becomes more diffuse and the maximum velocity decreases. Additionally, as back-arc spreading proceeds, the slab is shifted upward in response.
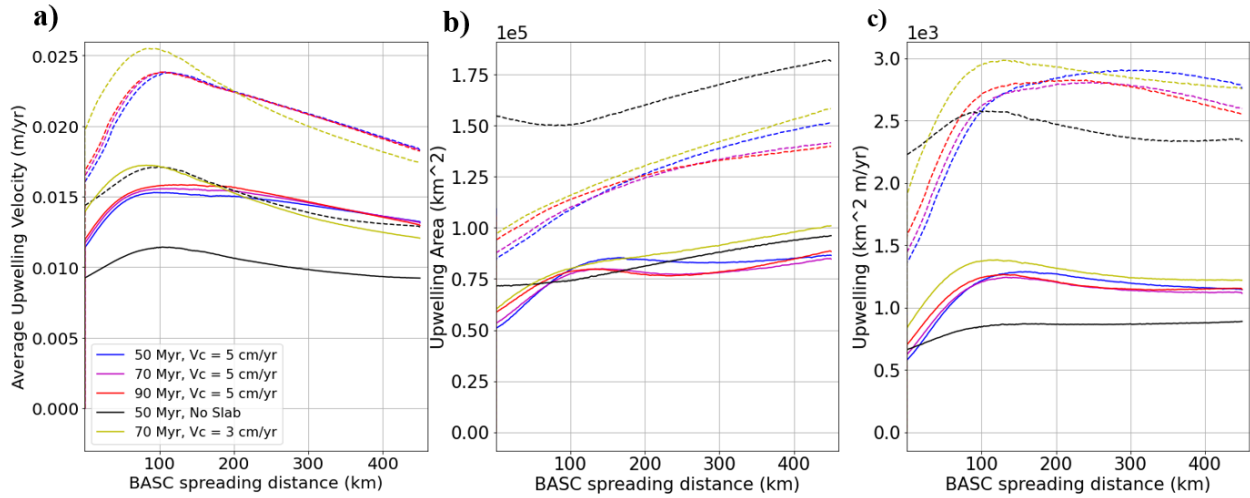

Figure 14) a: Plot of back-arc spreading distance versus average upwelling velocity. All models go through an initial velocity increase to a peak value that decays as the upwelling area increases. b: Plot of back-arc spreading distance versus upwelling area. Generally, the upwelling area increases as back-arc spreading proceeds. c: Plot of back-arc spreading distance versus total upwelling within the upwelling area. This is taken to be average upwelling velocity multiplied by the upwelling area. For every case, this seems to reach a steady-state between 100-250 km. The decay after reaching steady-state is the result of more material upwelling slower than 0.5 cm/yr and thus below our threshold used in the calculation. Dashed lines represent back-arc spreading rate of 5 cm/yr and solid lines represent 2.5 cm/yr.
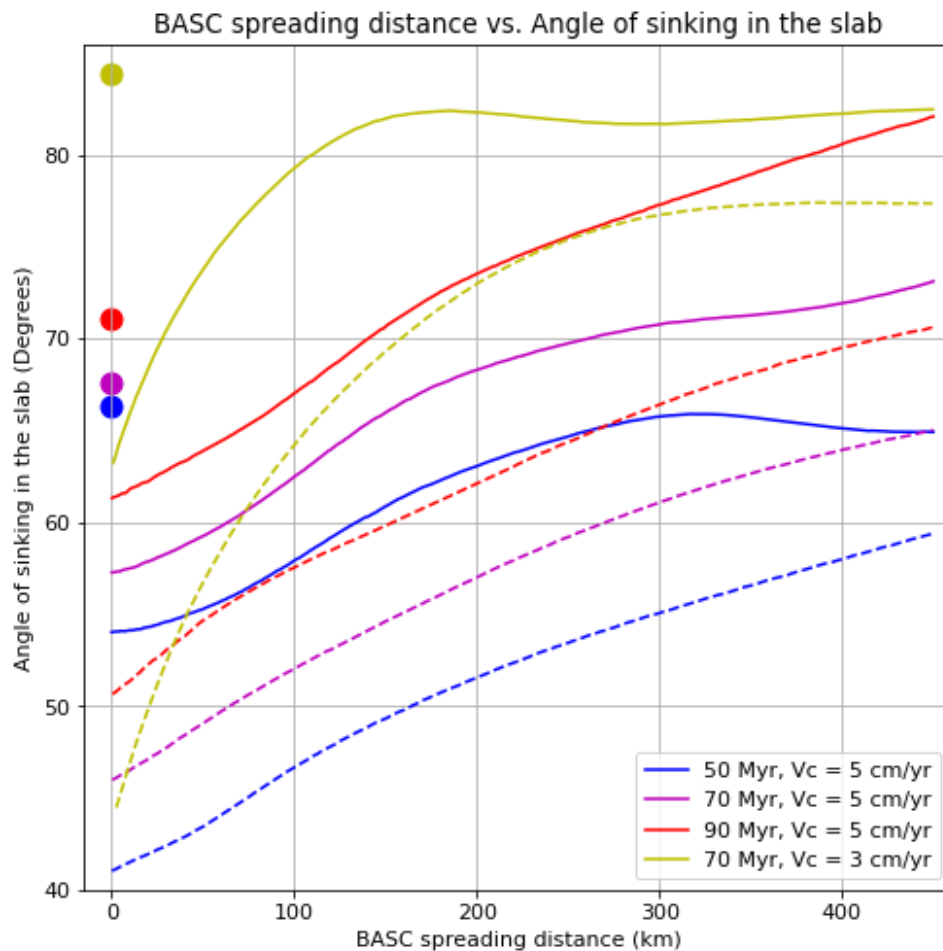
Figure 15) Plot of back-arc spreading distance versus angle of sinking in the slab. Dashed lines represent back-arc spreading rate of 5 cm/yr and solid lines represent 2.5 cm/yr. The colored dots indicate the angle of sinking prior to the initiation of the BASC and correspond to the slab age and convergence velocity of their respective color (e.g., the blue dot is for the 50 Myr and u_c=5 cm/yr model and applies to both the u_b=2.5 and u_b=5 cm/yr models). For every model after the BASC initiates, there is a rapid drop in the angle of sinking that gradually increases as the back-arc migrates further from the trench. Faster back-arc spreading corresponds to a larger drop in the angle of sinking.
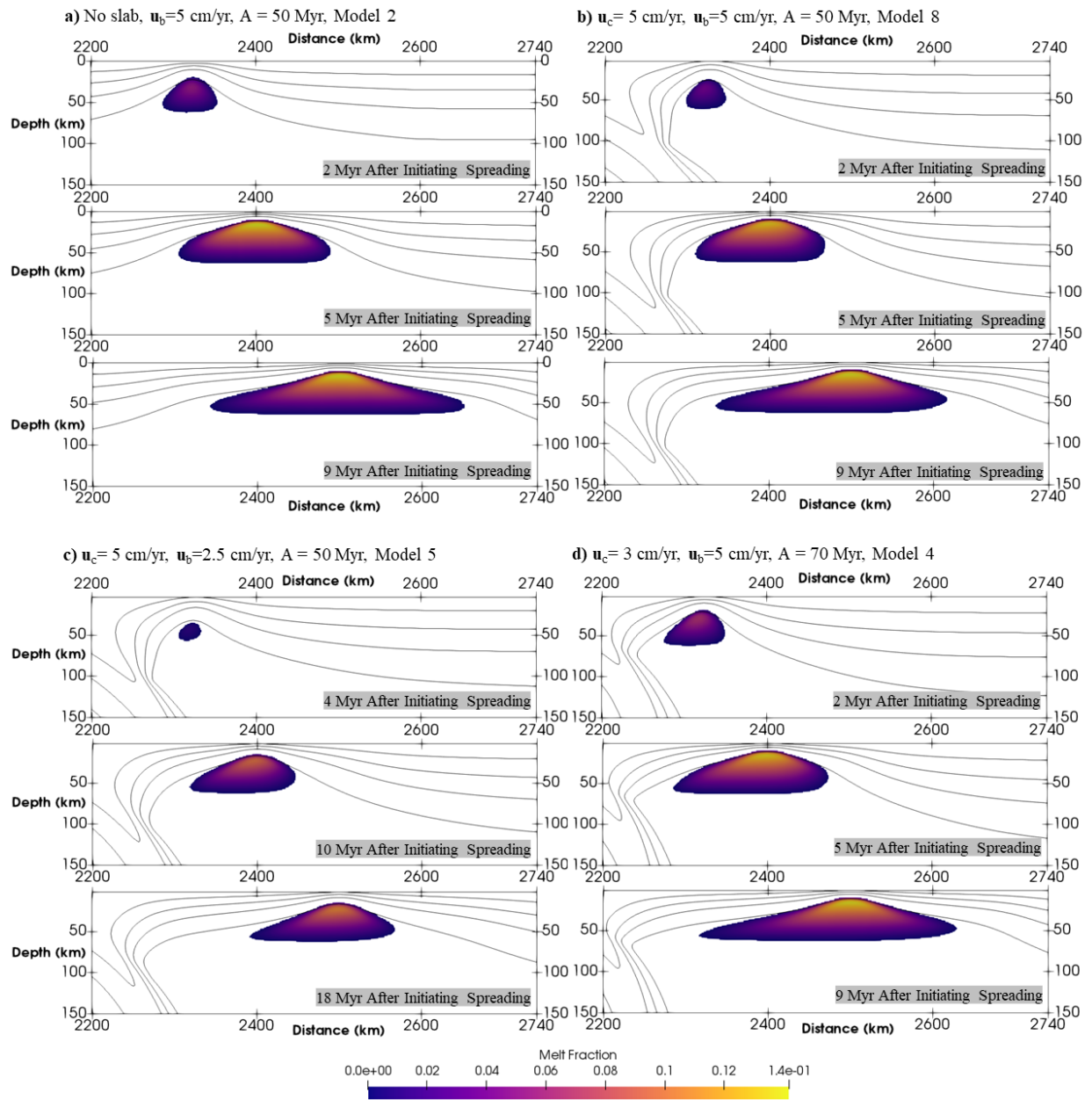
Figure 16) Evolution of the melt region through time. The black contours are temperature contours starting at 300 °C to 1200 °C in 300 °C increments. a: Model 2; b: Model 8; c: Model 5; d: Model 4. A primary control on melt formation is the back-arc spreading velocity, as the melt extent is nearly halved and also has a smaller total melt fraction. Compared to the MOR model (Model 8), the BASC models all develop an asymmetrical melt region due to the influence of the slab.
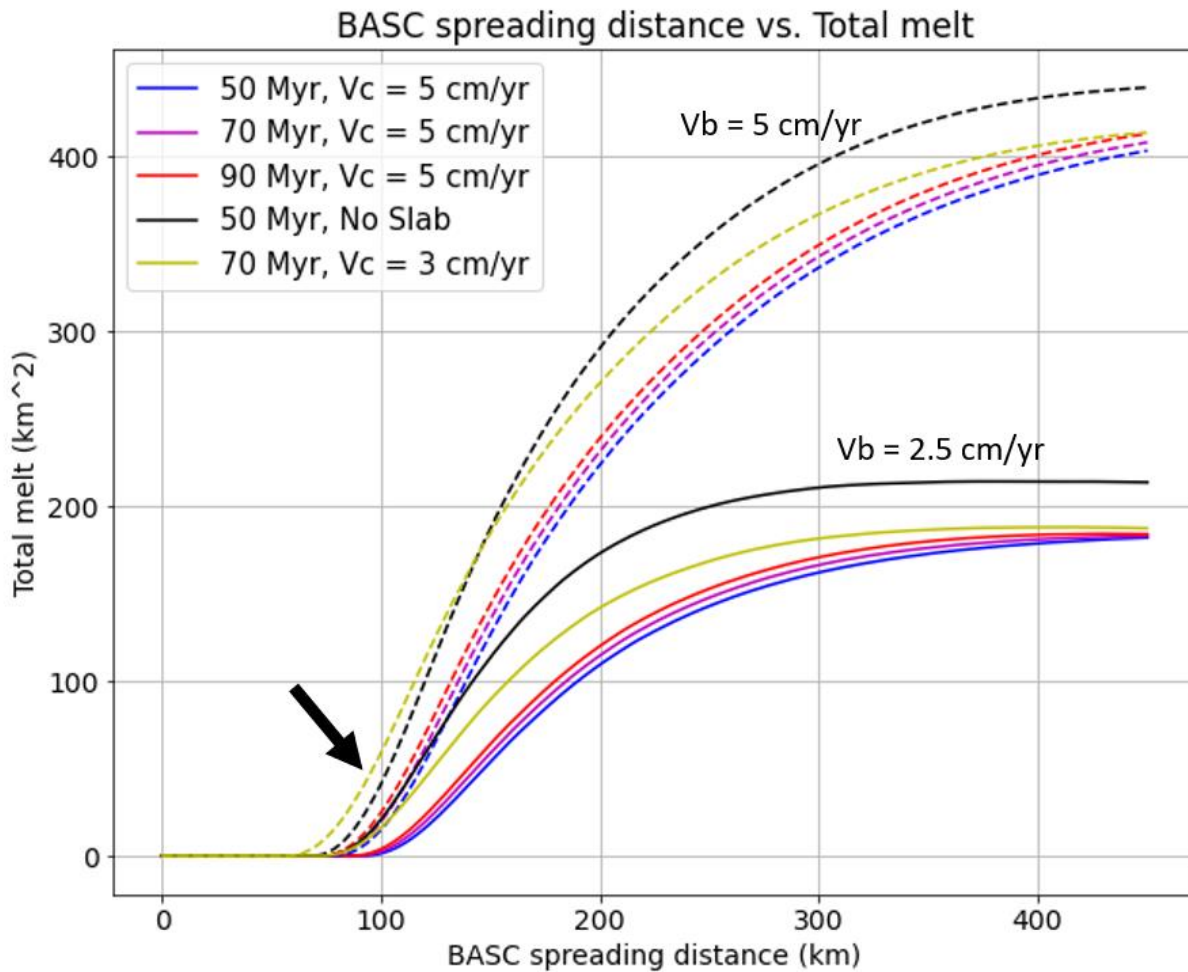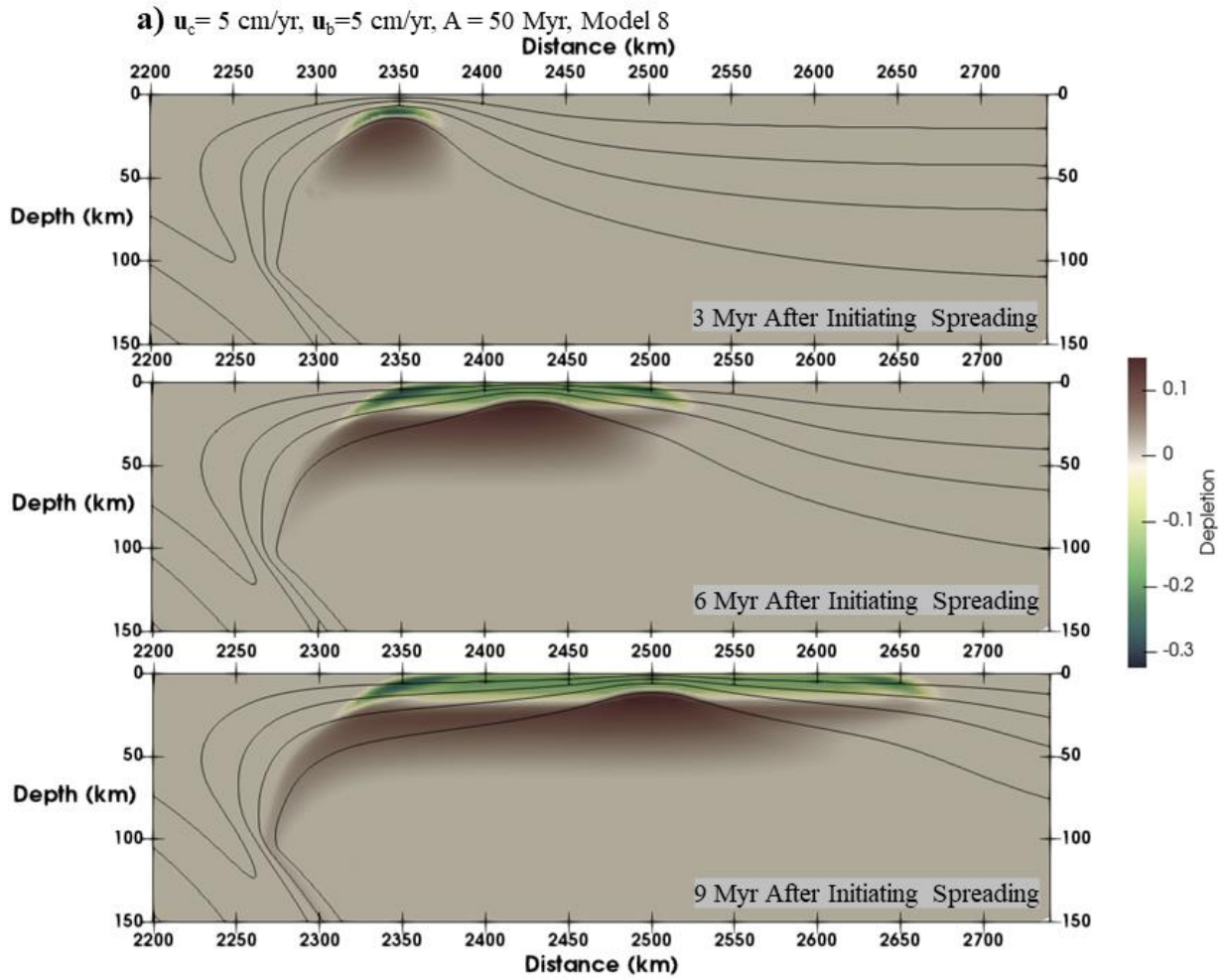
Figure 17) Plot of BASC spreading distance versus total melt present in each model. Dashed lines represent back-arc spreading rate of 5 cm/yr and solid lines represent 2.5 cm/yr. The MOR-style models (black lines, Models 1 and 2) evolve to have the largest melt fraction, however the 3 cm/yr convergence rate, 5 cm/yr back-arc spreading rate model initially develops melt faster (black arrow).

a) u_c = 5 cm/yr, u_b = 5 cm/yr, A = 50 Myr, Model 8

3 Myr After Initiating Spreading

6 Myr After Initiating Spreading
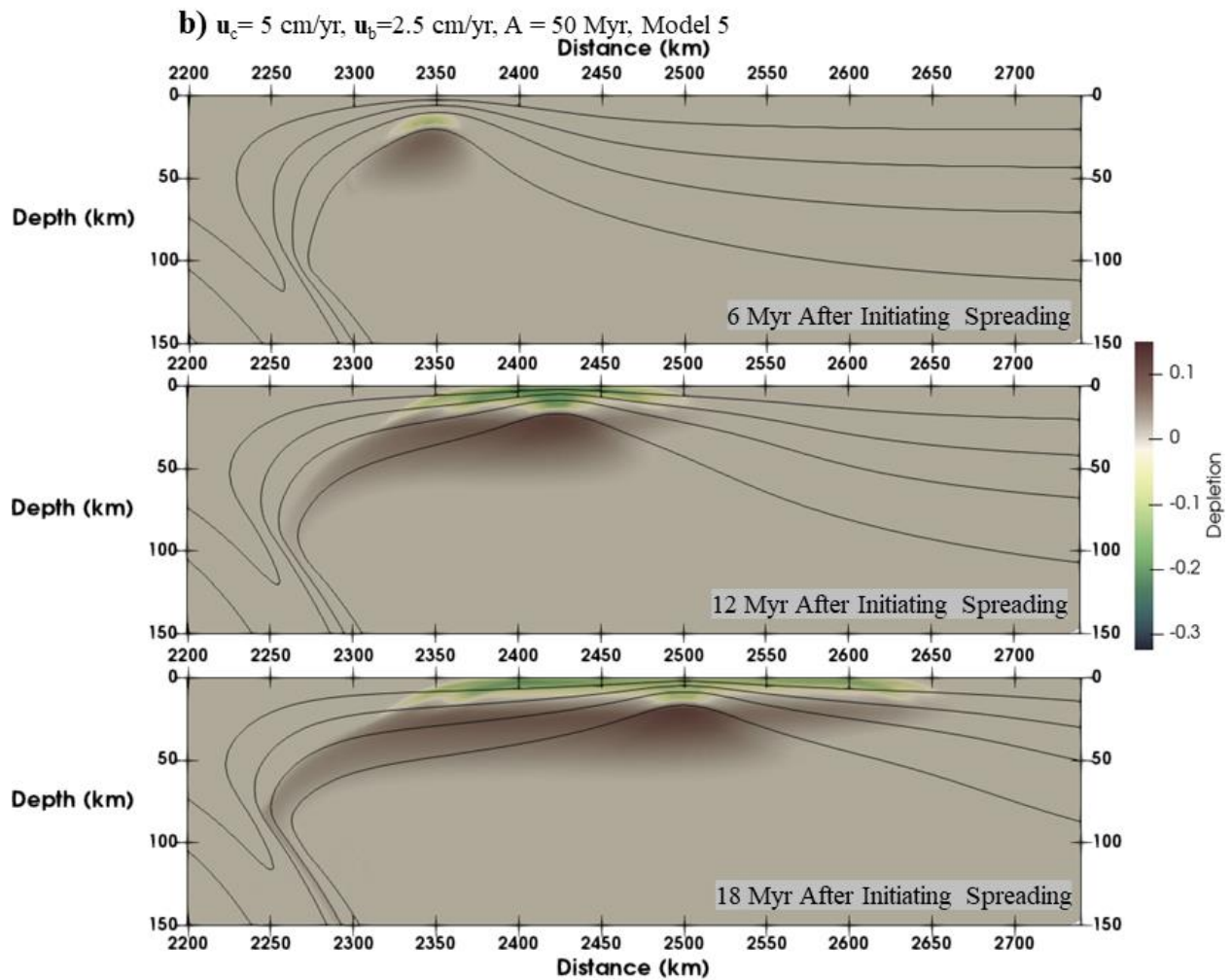
9 Myr After Initiating Spreading

Figure 18) Evolution of depletion in the BASC region through time in a: Model 8; b: Model 5. Green represents areas of enrichment (oceanic crust) and black represents areas of depletion. The enriched crust has a thickness that varies from 10-15 km thick in a, and 7-15 km thick in b. Additionally, the depleted mantle produced beneath the BASC, gets advected beneath the arc after ~150 km of back-arc spreading.
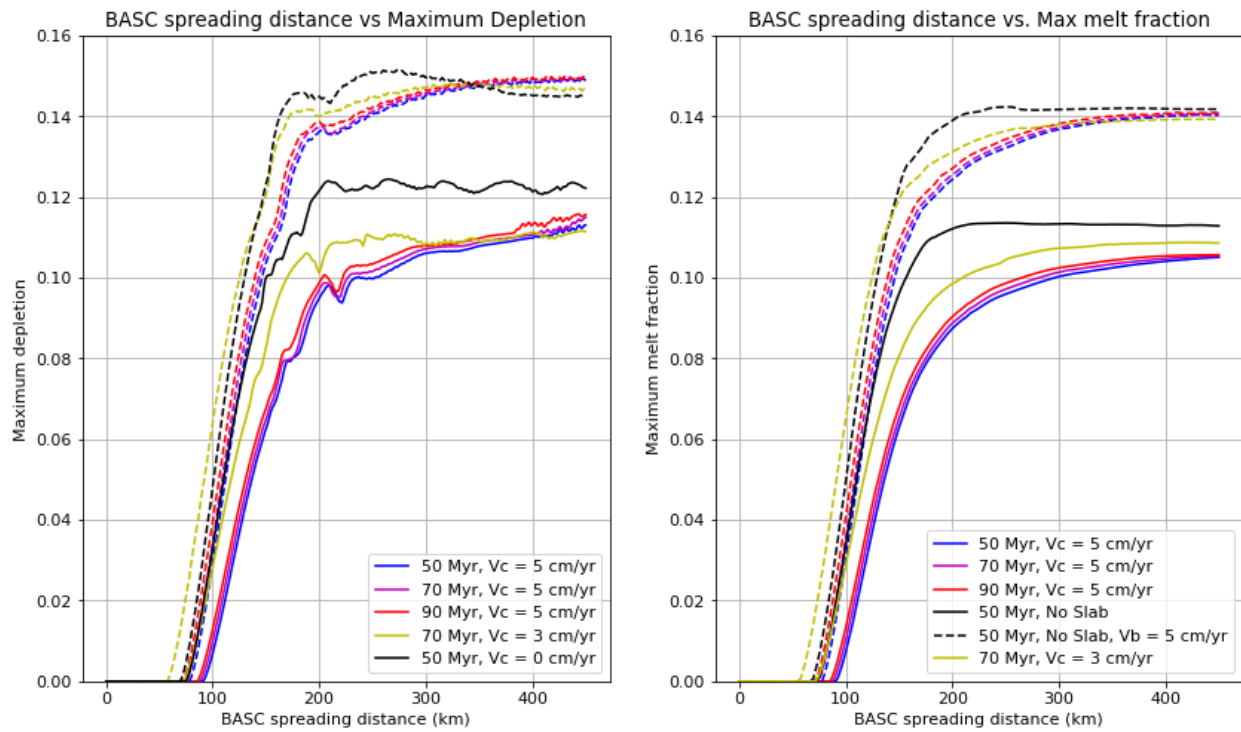
Figure 19) a) Plot of BASC spreading distance versus maximum depletion in the BASC region. b) Plot of BASC spreading distance versus maximum melt fraction. Dashed lines represent back-arc spreading rate of 2.5 cm/yr and solid lines represent 5 cm/yr. Maximum depletion and maximum melt fraction reaches a steady-state after ~200 km of spreading.
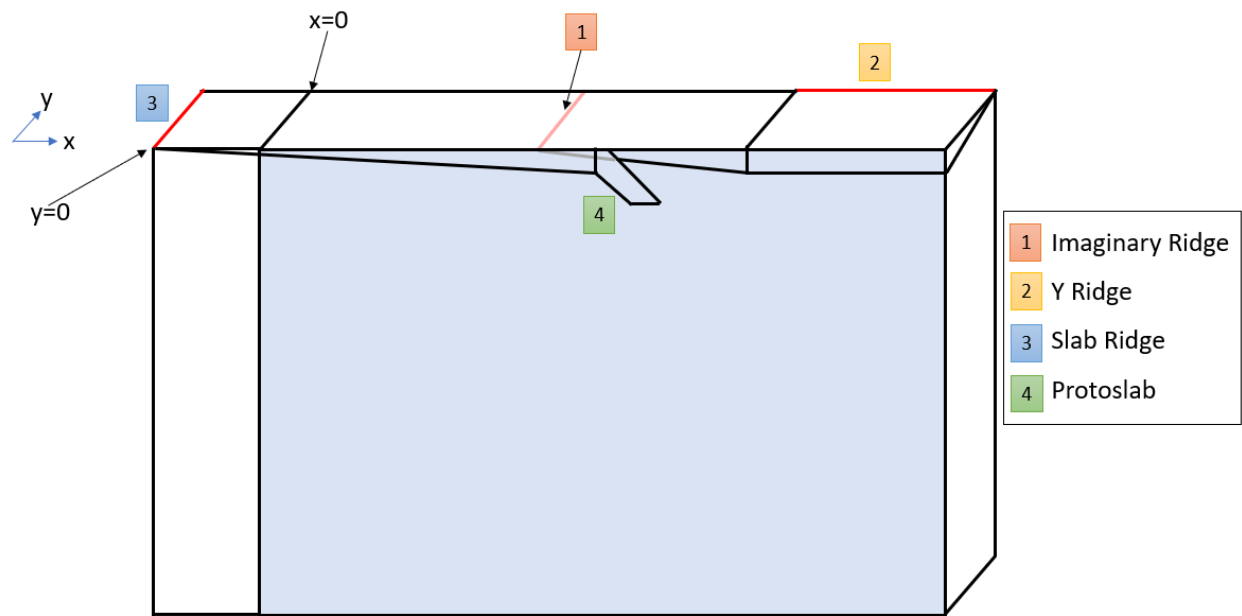
Figure A1) Schematic model set up using worldbuilder. Grey shaded region indicates the 'slice' through which our 2D model domain is taken. Features in the worldbuilder file are numbered. Red lines indicate the locations of ridges. Faded lines are overprinted by a subsequent feature.

Tables

Papers	Harmon & Blackman, 2010	Lin et al., 2010	Nakakuki & Mura, 2012	Hall et al., 2012	Magni, 2019
Focus region	Lau Basin -Tonga	Mariana	Generic	Generic	Generic
Equations	BA	BA	EBA	BA	BA
Melt Migration	Melt travels up only due to buoyancy	-	-	Melt fraction calculated	Melt fraction calculated
Melt Computation	Katz, 2003	-	-	Katz, 2003	Katz, 2003
Depletion	Calculated for each element using finite difference	-	-	Lagrangian Particle Method *	Tracer method – tracks all composition
Water in wedge	Gaussian column in wedge centered at arc	Schematically discussed – not included in model	-	0.1% H2O everywhere	Column of water in wedge with 0.1wt% and 1wt% models
Rheology	P-T dependent, not fluid dependent	P-T dependent, not fluid dependent	P-T, yield strength, and yielding history dependent (no fluid) above 300 km	T dependent, not fluid dependent	Stress and T dependent Mantle wedge has 10^20 Pa s to simulate fluids
Min Viscosity	Background viscosity, $A=10^{20}$ Pa s	minimum strain rate in viscosity laws is set to be 10^{-18} s^{-1}	~10^{17} Pa s	~10^{20} Pa s but not explicitly defined	Background viscosity, $A=10^{20}$ Pa s
Max Viscosity	10^{23} Pa s	$2*10^{27}$ Pa s	~10^{25} Pa s	10^{26} Pa s	In Lithosphere: 10^{23} Pa s
Geometry	Box	Box	Box	Box	3D Box
Model Width	800 km	660 km	10000 km	600 km	3300 km x 3960 km
Model Depth	600 km	610 km	2000 km	600 km	660 km
Slab behavior	Kinematic	Kinematic	Dynamic	Kinematic	Dynamic
Back arc behavior	Kinematic	Kinematic	Dynamic	Kinematic	Dynamic
Dimensionality	2D	2D	2D	2D	3D
Boundary Conditions	-	-	Free slip on all sides	-	-
Top	T = 0 C; Arc plate: fixed Arc side Back-arc plate: half-spreading rate Arc far Back-arc plate: full spreading rate	T = 0 C; Free slip in arc and back-arc, no slip in forearc	T = 0 C; Free slip	T = 0 C; Arc plate: fixed Arc side Back-arc plate: half-spreading rate Arc far Back-arc plate: full spreading rate	T = 0 C; free slip
Bottom	T = Tm+ adiabat; Stress free	dT/dx = 0;Inflow/outflow	dT/dx=0; Free slip	dT/dx = 0; Fixed v equal to subduction v	T = 1350 C; no slip
Sides	Left: T = half-space + adiabat; Stress Free Right: dT/dx = 0; Stress free	dT/dy = 0 at outflow, T fixed on wedge side inflow and trench side; Inflow/outflow Uniform far-field plate motion imposed on left side to 40 km depth	Insulating BC; Free slip	T = T(t); Right: Stress free Left: v equal to subduction v T	dT/dy or dT/dx = 0; free slip
Numerical Methods	Finite difference	Finite Volume	Finite Volume	Finite Element	Finite Element

Table 1) Table consisting of the different models of back-arc melting from different studies and how they are set up. There are broadly two styles of modelling, fully kinematic models that prescribe surface conditions to create a back-arc spreading center (Harmon & Blackman 2010; Lin et al., 2010; Hall et al., 2012) and fully dynamic models that set up conditions to promote a dynamically created back-arc spreading center (Nakakuki & Mura, 2012; Magni, 2019). Note all studies with melting use the Katz et al., 2003 formulation for melting.

Model Number	Convergence rate (cm/yr)	Back-arc spreading rate (cm/yr)	Slab Age at Trench (Myr)
Slow/Intermediate Velocity Models (Worked)			
1	*	2.5*	50*
2		5*	50*
3	3	2.5	70
4		5	70
5			50
6	5	2.5	70
7			90
8			50
9	5	5	70
10			90
Fast Velocity Models (Did Not Work)			
11			50
12	5	7.5	70
13			90
14			50
15	7	2.5	70
16			90
17			50
18	7	5	70
19			90
20			50
21	7	7.5	70
22			90
23			50
24	9	2.5	70
25			90
26			50
27	9	5	70
28			90
29			50
30	9	7.5	70
31			90

Table 2) Summary of modelling suite. It is divided into two broad categories of slow/intermediate models and fast models. During back-arc spreading, fast models are pulled through the shear zone, rendering them unsuitable for analysis. Values of convergence velocity selected as a reprehensive sample from Lallemand et al. (2005). Note that subduction zones with back-arc spreading centers typically have slabs older than ~50 Myr, which informs the in choice slab ages we model (Sdrolias and Muller, 2006).

* Models 1 and 2 have no slab and thus no convergence rate but have an initial overriding plate age of 50 Myr. Back-arc spreading rate in these models is instead Mid-ocean ridge spreading rate.

Quantity		Symbol		Value	Units
Constants					
Reference permeability		k_0		1e-7	m^2
Melt extraction depth		-		0	m
Freezing rate		-		0.005	yr^{-1}
Melting time scale for operator splitting		-		200	yr
Exponential melt weakening factor		α_ϕ		20	
Thermal expansion coefficient		α		3e-5	K^{-1}
Solid compressibility		κ_s		4.2e-12	Pa^{-1}
Thermal viscosity exponent		β		10	-
Reference shear viscosity		η_0		1e18	Pa s
Upper Mantle viscosity depth dependence slope		m_1		1.515e-2	km^{-1}
Lower Mantle viscosity depth dependence slope		m_2		2.269	km^{-1}
Depth dependent viscosity factor offset between Upper and Lower Mantle		b		-1.107e3	-
Mantle Potential Temperature		T_p		1570	K
Mass Fraction cpx		-		0.15	-
Overriding Plate age at Arc		-		50	Myr
Experimental Parameters					
Convergence Velocity		$\mathbf{u}_c$			cm/yr
Back-arc spreading velocity		$\mathbf{u}_b$			cm/yr
Slab age at trench		A			Myr

Table 3) Table of important variables used in models and their values. Unless otherwise noted, we use ASPECTs default values. Not all quantities have symbols.

References

Artemieva, I. M. (2023). Back-arc basins: A global view from geophysical synthesis and analysis. *Earth-Science Reviews*, *236*, 104242. https://doi.org/10.1016/j.earscirev.2022.104242

Bangerth, W., Dannberg, J., Fraters, M., Gassmoeller, R., Glerum, A., Heister, T., & Naliboff, J. (2021a). *ASPECT: Advanced Solver for Problems in Earth's ConvecTion, User Manual*. https://doi.org/10.6084/m9.figshare.4865333

Bangerth, W., Dannberg, J., Fraters, M., Gassmoeller, R., Glerum, A., Heister, T., & Naliboff, J. (2021b). *ASPECT v2.3.0* (v2.3.0). Zenodo. https://doi.org/10.5281/zenodo.5131909

Billen, M. I. (2017). Insights Into the Causes of Arc Rifting From 2-D Dynamic Models of Subduction. *Geophysical Research Letters*, *44*(21). https://doi.org/10.1002/2017GL075061

Billen, M. I., & Hirth, G. (2005). Newtonian versus non-Newtonian upper mantle viscosity: Implications for subduction initiation. *Geophysical Research Letters*, *32*(19), n/a-n/a. https://doi.org/10.1029/2005GL023457

Carbotte, S. M., & Canales, J. P. (2019). Tectonics: Seismic Structure at Mid-Ocean Ridges. In *Encyclopedia of Ocean Sciences* (pp. 455–471). Elsevier. https://doi.org/10.1016/B978-0-12-409548-9.10801-2

Cooper, L. B., Plank, T., Arculus, R. J., Hauri, E. H., Hall, P. S., & Parman, S. W. (2010). High-Ca boninites from the active Tonga Arc. *Journal of Geophysical Research*, *115*(B10), B10206. https://doi.org/10.1029/2009JB006367

Dannberg, J., Gassmöller, R., Grove, R., & Heister, T. (2019). A new formulation for coupled magma/mantle dynamics. *Geophysical Journal International*, ggz190. https://doi.org/10.1093/gji/ggz190

Dannberg, J., & Heister, T. (2016). Compressible magma/mantle dynamics: 3-D, adaptive simulations in ASPECT. *Geophysical Journal International*, *207*(3), 1343–1366. https://doi.org/10.1093/gji/ggw329

Fraters, M. (2020). *The Geodynamic World Builder* (v0.3.0). Zenodo. https://doi.org/10.5281/zenodo.3900603

Fraters, M., Thieulot, C., van den Berg, A., & Spakman, W. (2019). The Geodynamic World Builder: A solution for complex initial conditions in numerical modeling. *Solid Earth*, *10*(5), 1785–1807. https://doi.org/10.5194/se-10-1785-2019

Garfunkel, Z., Anderson, C. A., & Schubert, G. (1986). Mantle circulation and the lateral migration of subducted slabs. *Journal of Geophysical Research: Solid Earth*, *91*(B7), 7205–7223. https://doi.org/10.1029/JB091iB07p07205

Grevemeyer, I., Kodaira, S., Fujie, G., & Takahashi, N. (2021). Structure of oceanic crust in back-arc basins modulated by mantle source heterogeneity. *Geology*, *49*(4), 468–472. https://doi.org/10.1130/G48407.1

Hall, P. S., Cooper, L. B., & Plank, T. (2012). Thermochemical evolution of the sub-arc mantle due to back-arc spreading. *Journal of Geophysical Research: Solid Earth*, *117*(B2), n/a-n/a. https://doi.org/10.1029/2011JB008507

Harmon, N., & Blackman, D. K. (2010). Effects of plate boundary geometry and kinematics on mantle melting beneath the back-arc spreading centers along the Lau Basin. *Earth and Planetary Science Letters*, *298*(3–4), 334–346. https://doi.org/10.1016/j.epsl.2010.08.004

Heister, T., Dannberg, J., Gassmöller, R., & Bangerth, W. (2017). High Accuracy Mantle Convection Simulation through Modern Numerical Methods. II: Realistic Models and Problems. *Geophysical Journal International*, *210*(2), 833–851. https://doi.org/10.1093/gji/ggx195

Hochstaedter, A. G., Gill, J. B., Taylor, B., Ishizuka, O., Yuasa, M., & Monta, S. (2000). Across-arc geochemical trends in the Izu-Bonin arc: Constraints on source composition and mantle melting. *Journal of Geophysical Research: Solid Earth*, *105*(B1), 495–512. https://doi.org/10.1029/1999JB900125

Katz, R. F., Spiegelman, M., & Langmuir, C. H. (2003). A new parameterization of hydrous mantle melting. *Geochemistry, Geophysics, Geosystems*, *4*(9), n/a-n/a. https://doi.org/10.1029/2002GC000433

Kelley, K. A., Plank, T., Grove, T. L., Stolper, E. M., Newman, S., & Hauri, E. (2006). Mantle melting as a function of water content beneath back-arc basins. *Journal of Geophysical Research*, *111*(B9), B09208. https://doi.org/10.1029/2005JB003732

Kronbichler, M., Heister, T., & Bangerth, W. (2012). High Accuracy Mantle Convection Simulation through Modern Numerical Methods. *Geophysical Journal International*, *191*, 12–29. https://doi.org/10.1111/j.1365-246X.2012.05609.x

Lallemand, S., Heuret, A., & Boutelier, D. (2005). On the relationships between slab dip, back-arc stress, upper plate absolute motion, and crustal nature in subduction zones. *Geochemistry, Geophysics, Geosystems*, *6*(9), n/a-n/a. https://doi.org/10.1029/2005GC000917

Langmuir, C. H., Bézos, A., Escrig, S., & Parman, S. W. (2006). Chemical systematics and hydrous melting of the mantle in back-arc basins. In D. M. Christie, C. R. Fisher, S.-M. Lee, & S. Givens (Eds.), *Geophysical Monograph Series* (Vol. 166, pp. 87–146). American Geophysical Union. https://doi.org/10.1029/166GM07

Li, S., Suo, Y., Li, X., Liu, B., Dai, L., Wang, G., Zhou, J., Li, Y., Liu, Y., Cao, X., Somerville, I., Mu, D., Zhao, S., Liu, J., Meng, F., Zhen, L., Zhao, L., Zhu, J., Yu, S., Zhang, G. (2018). Microplate tectonics: New insights from micro-blocks in the global oceans, continental margins and deep mantle. *Earth-Science Reviews*, *185*, 1029–1064. https://doi.org/10.1016/j.earscirev.2018.09.005

Lin, S.-C., Kuo, B.-Y., & Chung, S.-L. (2010). Thermomechanical models for the dynamics and melting processes in the Mariana subduction system. *Journal of Geophysical Research*, *115*(B12), B12403. https://doi.org/10.1029/2010JB007658

Magni, V. (2019). The effects of back-arc spreading on arc magmatism. *Earth and Planetary Science Letters*, *519*, 141–151. https://doi.org/10.1016/j.epsl.2019.05.009

McKenzie, D. (1984). The Generation and Compaction of Partially Molten Rock. *Journal of Petrology*, *25*(3), 713–765. https://doi.org/10.1093/petrology/25.3.713

Nakakuki, T., & Mura, E. (2013a). Dynamics of slab rollback and induced back-arc basin formation. *Earth and Planetary Science Letters*, *361*, 287–297. https://doi.org/10.1016/j.epsl.2012.10.031

Scholz, C. H., & Campos, J. (1995). On the mechanism of seismic decoupling and back arc spreading at subduction zones. *Journal of Geophysical Research: Solid Earth*, *100*(B11), 22103–22115. https://doi.org/10.1029/95JB01869

Sdrolias, M., & Müller, R. D. (2006). Controls on back-arc basin formation. *Geochemistry, Geophysics, Geosystems*, *7*(4), 2005GC001090. https://doi.org/10.1029/2005GC001090

Sim, S. J., Spiegelman, M., Stegman, D. R., & Wilson, C. (2020). The influence of spreading rate and permeability on melt focusing beneath mid-ocean ridges. *Physics of the Earth and Planetary Interiors*, *304*, 106486. https://doi.org/10.1016/j.pepi.2020.106486

Tatsumi, Y. (1986). Formation of the volcanic front in subduction zones. *Geophysical Research Letters*, *13*(8), 717–720. https://doi.org/10.1029/GL013i008p00717

Wilson, C. R., Spiegelman, M., van Keken, P. E., & Hacker, B. R. (2014). Fluid flow in subduction zones: The role of solid rheology and compaction pressure. *Earth and Planetary Science Letters*, *401*, 261–274. https://doi.org/10.1016/j.epsl.2014.05.052

Woodhead, J., Eggins, S., & Gamble, J. (1993). High field strength and transition element systematics in island arc and back-arc basin basalts: Evidence for multi-phase melt extraction and a depleted mantle wedge. *Earth and Planetary Science Letters*, *114*(4), 491–504. https://doi.org/10.1016/0012-821X(93)90078-N